The Influence of CO₂ Forcing on North American Monsoon Moisture Surges✎

SALVATORE PASCALE

NOAA/Geophysical Fluid Dynamics Laboratory, and Program in Atmospheric and Oceanic Sciences, Princeton University, Princeton, New Jersey

SARAH B. KAPNICK

NOAA/Geophysical Fluid Dynamics Laboratory, Princeton, New Jersey

SIMONA BORDONI

California Institute of Technology, Pasadena, California

THOMAS L. DELWORTH

NOAA/Geophysical Fluid Dynamics Laboratory, Princeton, New Jersey

ABSTRACT

Widespread multiday convective bursts in the southwestern United States during the North American monsoon are often triggered by Gulf of California moisture surges (GoC surges). However, how GoC surges, and the amount and intensity of associated precipitation, will change in response to CO_2-induced warming remains little known, not least because the most widely available climate models do not currently resolve the relevant mesoscale dynamics because of their coarse resolution (100 km or more). In this study, a 50-km-resolution global coupled model is used to address this question. It is found that the mean number of GoC surge events remains unchanged under CO_2 doubling, but intermediate-to-high intensity surge-related precipitation tends to become less frequent, thus reducing the mean summertime rainfall. Low-level moisture fluxes associated with GoC surges as well as their convergence over land to the east of the GoC intensify, but the increases in low-level moisture are not matched by the larger increments in the near-surface saturation specific humidity because of amplified land warming. This results in a more unsaturated low-level atmospheric environment that disfavors moist convection. These thermodynamic changes are accompanied by dynamic changes that are also detrimental to convective activity, with the midlevel monsoonal ridge projected to expand and move to the west of its present-day climatological maximum. Despite the overall reduction in precipitation, the frequency of very intense, localized daily surge-related precipitation in Arizona and surrounding areas is projected to increase with increased precipitable water.

1. Introduction

Convective activity developing during the summertime North American monsoon (NAM; e.g., Douglas et al. 1993; Adams and Comrie 1997; Higgins et al. 1997) accounts for a substantial fraction of the total annual precipitation in the southwestern United States (30%–50%) and northwestern Mexico (60%–80%). In these regions, the most severe rainfall events occur during the monsoon season, typically covering the period from July to September, and can cause flooding and life-threatening flash floods (Crimmins 2006; Ralph et al. 2014; Moore et al. 2015; Yang et al. 2017). Therefore, understanding the impact of increasing atmospheric greenhouse gas concentrations on precipitation extremes, in addition to that on mean rainfall, is of strategic importance for hazard preparedness, water resources, and conservation planning in the region (Ray et al. 2007).

✎ Supplemental information related to this paper is available at the Journals Online website: https://doi.org/10.1175/JCLI-D-18-0007.s1.

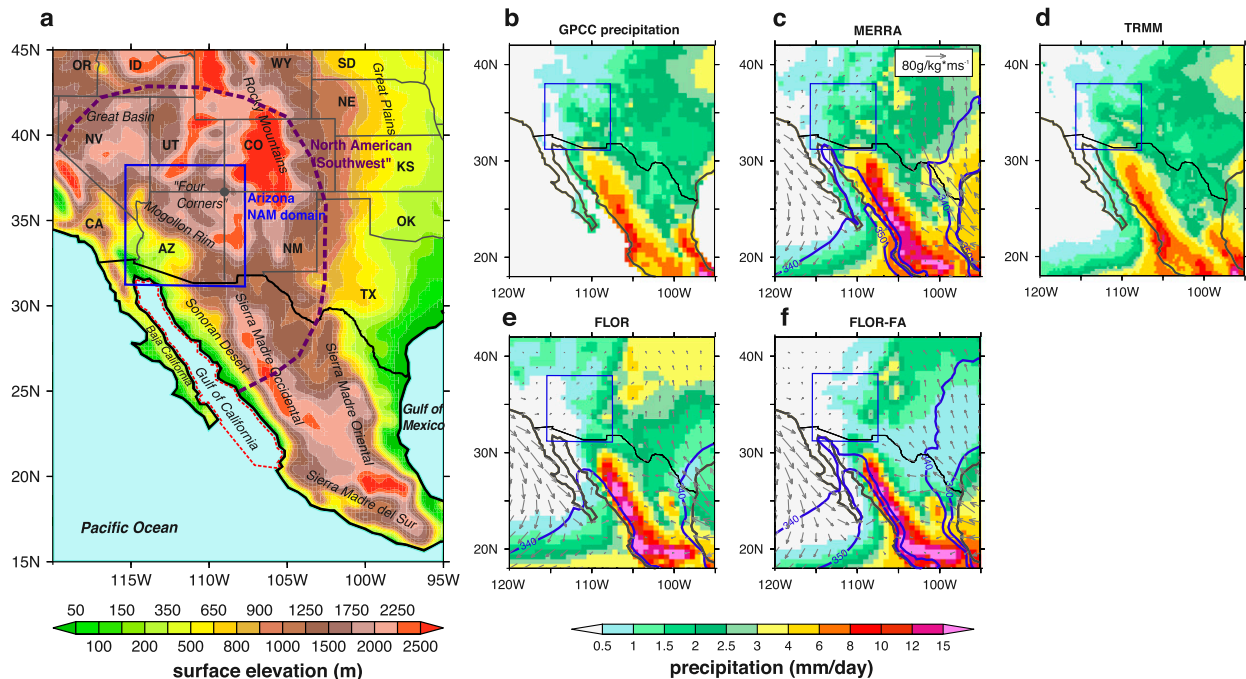*Corresponding author*: Salvatore Pascale, salvatore.pascale@noaa.gov

FIG. 1. (a) North American monsoon region and surroundings, with topographical features and main locations mentioned in text. The dashed red line defines the GoC area over which near-surface alongshore wind anomalies are considered for the PC analysis. The dashed line indicates the region referred to as the North American Southwest or simply the Southwest, while the blue rectangle delimits the Arizona domain used to estimate area-averaged precipitation; (b) July–August precipitation in GPCC v6; (c)–(f) July–August precipitation in MERRA, TRMM, FLOR, and FLOR-FA, respectively. Blue contours in (c), (e), and (f) indicate isolines of 10-m moist static energy (340 and 350 kJ kg^{-1}) and arrows indicate the 10-m moisture flux.

Convection associated with the NAM arises from complex interactions between local topographical features (Fig. 1a) and synoptic, larger-scale forcing (e.g., Kiladis and Hall-McKim 2004; Lorenz and Hartmann 2006; Jiang and Lau 2008; Pascale and Bordoni 2016). This makes its simulation challenging for general circulation models [GCMs; e.g., those participating in phases 3 and 5 of the Coupled Model Intercomparison Project (CMIP3 and CMIP5, respectively); Meehl et al. 2007; Taylor et al. 2012]. For example, Liang et al. (2008) and Geil et al. (2013) show that many of the CMIP3 and CMIP5 GCMs struggle to reproduce a realistic NAM over the southwestern United States and northwestern Mexico (henceforth, the North American Southwest, Fig. 1a). This deficiency is due to several factors, such as an inadequate (or missing) representation of the Gulf of California (GoC) and other local topographical features, difficulties in realistically simulating the diurnal cycle of convective precipitation (Lee et al. 2007a,b), systematic sea surface temperature (SST) biases (Meyer and Jin 2016; Pascale et al. 2017), and an inadequate simulation of both eastern Pacific tropical cyclones (Camargo 2013) and of the seasonal movement of the North Atlantic subtropical high (Geil et al. 2013; Ryu

and Hayhoe 2014). Given these issues, it is not surprising that GCMs disagree even on the sign of the NAM precipitation response to increased greenhouse gas forcing in the North American Southwest (e.g., Fig. 7 of Cook and Seager 2013). Thanks to a higher horizontal resolution, regional climate models (RCMs) generally improve the simulation of mesoscale circulation features that are key to the NAM (e.g., Castro et al. 2007a,b), but they tend to maintain the same biases found in the GCM-generated forcing datasets used to provide them with lateral boundary conditions (e.g., Bukovsky et al. 2013; Meyer and Jin 2016). Consequently, their performance is inexorably dependent on the skills of the GCMs to reproduce a realistic large-scale circulation in present and future climate (Mo et al. 2005).

We have recently shown how the Forecast-Oriented Low Ocean Resolution model (FLOR; Vecchi et al. 2014), a global coupled model at surge-permitting horizontal resolution of 50 km, provides an improved representation of the monsoon (Figs. 1b–e) and its synoptic-scale variability (Pascale et al. 2016). Under CO_2 doubling and when SST biases are minimized (Pascale et al. 2017), this model projects a robust reduction in mean monsoonal precipitation, against consensus in CMIP3 and CMIP5

models that instead suggest an early-to-late redistribution of summertime rainfall (e.g., Seth et al. 2011; Cook and Seager 2013; Torres-Alavez et al. 2014; Maloney et al. 2014). Pascale et al. (2017) focused on mean changes, that is, changes in monthly means, without examining the impact of global warming on the synoptic-scale processes controlling precipitation in the NAM region. Among these processes, Gulf of California moisture surges (henceforth referred to as GoC surges; e.g., Hales 1972; Brenner 1974; Douglas et al. 1993; Stensrud et al. 1997; Zehnder 2004; Higgins et al. 2004; Rogers and Johnson 2007; Svoma 2010; Newman and Johnson 2012, 2013; Mejia et al. 2016) have been shown to significantly modulate the intensity and extent of NAM convection, especially in Arizona and surrounding areas[1] (Fig. 1a). In this region, intense heating over the elevated terrains triggers convection at almost daily frequency (e.g., Balling 1987; King and Balling 1994). However, larger-scale forcing is necessary to provide a thermodynamically and dynamically favorable environment and allow deep convective plumes to propagate westward and organize themselves into mesoscale convective systems. GoC surges provide one such synoptic-scale forcing by increasing the low-level moisture to overcome entrainment of drier midtropospheric air (Adams and Souza 2009). Most of the summertime precipitation in Arizona occurs during days of enhanced low-level southeasterly flow over the GoC (~70%; Becker and Berbery 2008; Pascale and Bordoni 2016), but surge events often happen simultaneously with the passage of upper-level inverted troughs (e.g., Bieda et al. 2009; Finch and Johnson 2010), which are another important synoptic-scale forcing. The remaining nearly 30% occur during nonsurge periods (see Table 2), and it can be due to convection primarily forced by the terrain diurnal heating (i.e., precipitation is phase-locked to the terrain) or by other synoptic-scale disturbances that can provide easterly or northeasterly flow at midlevels such as upper-level inverted troughs.

Knowing how GoC surges are impacted by anthropogenic climate change is thus key to understanding how the frequency and intensity of NAM thunderstorm events may change in the coming decades. Specifically, here we aim to achieve the following:

- Test the capability of the 50-km horizontal resolution FLOR GCM to realistically represent the relationship

between GoC surges, synoptic forcing, and the intensity of the associated precipitation
- Investigate changes in GoC surges and the intensity of associated precipitation in response to CO_2 doubling

In this paper, we will primarily focus on synoptic-scale events that are associated with GoC moisture surges, whose mesoscale and larger-scale forcings are reasonably captured by FLOR (Pascale et al. 2016). We will not deal with subdaily extreme rainfall (e.g., Prein et al. 2017a,b) since FLOR, like other GCMs that feature parameterized convection (Moorthi and Suarez 1992), has limitations in capturing the diurnal cycle of summertime convection in the NAM region (Lee et al. 2007a,b) and of the development of mesoscale convective systems off the Arizona high terrains.

The paper will be organized as follows. In section 2, we give a brief overview of the Geophysical Fluid Dynamics Laboratory (GFDL) model and other datasets used in this study and describe our methodology to identify GoC surges. In section 3, we evaluate the relationship between GoC surges and precipitation intensity in model simulations, and in section 4 we investigate the impact of CO_2 forcing on GoC surges. A critical discussion of our results and a summary are provided in section 5 and section 6, respectively.

2. Data and methods

a. Reanalyses and observations

We use the reanalyses provided by the European Centre for Medium-Range Weather Forecasts (ECMWF) interim reanalysis (ERA-Interim, herein ERA-I; Dee et al. 2011; Berrisford et al. 2011a). The ERA-I atmospheric model has 60 vertical levels and a horizontal resolution of about 79 km (Berrisford et al. 2011b), which is sufficient to resolve the GoC and other important topographical features of the NAM region. Total precipitation, 10-m wind, and 500-hPa geopotential height and winds are obtained for the period 1979–2014 at 6-h time frequency and then averaged to construct daily means. This removes diurnal variations while retaining variability associated with synoptic disturbances. We also use the National Aeronautics and Space Administration Goddard Space Flight Center (GSFC) Modern-Era Retrospective Analysis for Research and Applications (MERRA; Rienecker et al. 2011) to verify consistency of results from the two different reanalyses. MERRA has vertical and horizontal resolutions (72 levels and 0.5° latitude × 0.67° longitude grid spacing) that are comparable to that of ERA-I. Variables are obtained at daily frequency for the period 1979–2010.

---

[1] In the following we will refer to the rectangular region defined in Fig. 1a as "Arizona," even though this encompasses not only the state of Arizona but also the closely surrounding areas of California, Nevada, Utah, Colorado, and New Mexico.

TABLE 1. Description of the coupled runs used in this study.

Experiment	Years	Radiative forcing/boundary conditions	Purpose
CTRL_FLOR	200	CO_2 constant at 1990 levels	Control run
CTRL_FLOR-FA	200	CO_2 constant at 1990 levels	Control run with flux adjustment; reduce SST biases
2CO₂_FLOR	300	CO_2 doubles in 70 years, then constant	CO_2 forcing
2CO₂_FLOR-FA	300	CO_2 doubles in 70 years, then constant	CO_2 forcing with flux adjustment; reduce SST biases

For total precipitation, we additionally use (i) the National Oceanic and Atmospheric Administration (NOAA) Climate Prediction Center (CPC) U.S. Unified Gauge-Based Analysis (Chen et al. 2008a,b), available at 0.25° × 0.25° horizontal resolution and daily time resolution;[2] (ii) the Global Precipitation Climatology Centre, version 6 (GPCC v6), dataset (Schneider et al. 2014), based on statistically interpolated in situ rain measurements covering all land areas (0.5° × 0.5° horizontal resolution) for the period 1901–2010 at monthly temporal resolution,[3] and (iii) the daily accumulated precipitation generated from the research-quality Tropical Rainfall Measuring Mission (TRMM) Multisatellite Precipitation Analysis[4] 3B42 (Huffman et al. 2007).

b. Model and experiments

Numerical simulations are performed with the coupled FLOR model (Vecchi et al. 2014), developed at the NOAA GFDL. FLOR has been derived from the GFDL Climate Model, version 2.5 (CM2.5; Delworth et al. 2012), which has been successfully used for studies of regional hydroclimatic variability and change (e.g., Kapnick et al. 2014; Delworth and Zeng 2014; Delworth et al. 2016; Zhang et al. 2016; Pascale et al. 2016, 2017). FLOR and CM2.5 are identical (horizontal resolution of 0.5° × 0.5° in the atmosphere–land model and 32 vertical levels) but differ in horizontal resolution in the ocean–sea ice components (~1° × 1°, with meridional resolution of ⅓° near the equator in FLOR, vs ~0.25° × 0.25°, with gridbox sizes ranging from 28 km at the equator to 8 km in polar regions in CM2.5). The flux-adjusted version of FLOR (FLOR-FA) is also available. In FLOR-FA, climatological adjustments are made to FLOR surface fluxes of momentum, enthalpy, and freshwater in order to bring the model ocean surface climatology closer to the observed 1979–2012 climatology (Table 1), substantially reducing the negative SST biases in the subtropical and extratropical Atlantic and Pacific Oceans.

The availability of simulations without and with flux adjustment allows us to evaluate the effects of these SST biases, which have a substantial impact on the response of the mean NAM to increased CO_2 (Pascale et al. 2017).

Control runs for FLOR (CTRL_FLOR) and FLOR-FA (CTRL_FLOR-FA) are obtained from a 200-yr simulation with atmospheric composition (greenhouse gases and aerosols) and external forcing (solar irradiance) at 1990 levels (Table 1). In the forced experiments (2CO₂_FLOR and 2CO₂_FLOR-FA), atmospheric CO_2 concentration starts at 1990 levels (≈354 ppm), increases at a rate of 1% per year, doubles in 70 years, and it is then held constant as the model runs for an additional 230 years. For our analysis we take the last 200 years of the whole run. The mean global surface temperature increase associated with the steady-state 2CO₂_FLOR and 2CO₂_FLOR-FA climates is approximately +2 K.

Overall, flux adjustment in FLOR has a large impact on summertime precipitation over North America. In particular, it reduces the precipitation climatology root-mean-square error (RMSE) over the U.S. region (25°–50°N, 60°–130°W) by 18.3% in October–March and by 43.4% in April–September as compared to GPCC. The large impact of SST biases (especially in the Atlantic Ocean) on the North American hydroclimate arises from biases in the large-scale North Atlantic subtropical high induced by cooler tropical Atlantic Ocean (e.g., Wang et al. 2007). In summer, a cooler subtropical Atlantic Ocean in FLOR relative to FLOR-FA induces a stronger North Atlantic subtropical high, particularly in its southwestern lobe over the Gulf of Mexico. As explained in Geil et al. (2013), this is also the main reason for the NAM "retreat" problem, which is also seen in FLOR, and that causes an unrealistic seasonal cycle. Importantly for this study, FLOR-FA allows for a more realistic representation of the high near-surface moist static energy tongue along the GoC and the GoC low-level jet (Fig. 1) and of the monsoonal ridge (Fig. 3 in Pascale et al. 2016), and it better resolves GoC surges and their time variability (Pascale et al. 2016). However, FLOR-FA features a dry bias over western Arizona (see also Figs. 1d,e and Table 2), which may arise because the northernmost GoC is not resolved in FLOR. This may artificially reduce precipitation in this region, given the key role played by the

---

[2] Available online at http://www.esrl.noaa.gov/psd/data/gridded/data.unified.daily.conus.html.

[3] Available online at the NOAA/Physical Sciences Division Climate and Weather Data website www.esrl.noaa.gov/psd/data/.

[4] Available online at https://pmm.nasa.gov/data-access/downloads/trmm.

TABLE 2. Values of the total number of surge events, mean number of surges per year n_{ns}, area-averaged precipitation $\langle P \rangle$ (mm day^{-1}), surge-related precipitation $\langle P_{su} \rangle$ (mm day^{-1}), and nonsurge-related precipitation $\langle P_{ns} \rangle$ (mm day^{-1}) during 21 Jun–30 Sep for the datasets used in this study. Area averages are computed over the Arizona domain shown in Fig. 1. Standard deviations associated with interannual variability are also shown. For CPC and TRMM, surge days are defined on the basis of ERA-I wind field.

Dataset	Years	Total events	n_{su}	$\langle P \rangle$	$\langle P_{su} \rangle$	$\langle P_{ns} \rangle$	$\langle P_{su} \rangle / \langle P \rangle$
ERA-I	1979–2014	558	15.5 ± 2.0	1.04 ± 0.46	0.76 ± 0.36	0.27 ± 0.15	73%
MERRA	1979–2010	489	15.3 ± 1.5	1.39 ± 0.37	1.03 ± 0.26	0.36 ± 0.15	74%
CPC	1979–2006	—	—	1.25 ± 0.32	0.90 ± 0.25	0.34 ± 0.13	72%
TRMM	1998–2017	—	—	1.28 ± 0.32	0.90 ± 0.24	0.37 ± 0.18	70%
FLOR	200	2800	14.0 ± 2.0	1.19 ± 0.48	0.81 ± 0.34	0.38 ± 0.23	68%
2CO$_2$_FLOR	101–300	2804	14.0 ± 2.4	1.19 ± 0.47	0.81 ± 0.34	0.38 ± 0.23	68%
FLOR-FA	200	3241	16.2 ± 2.2	0.65 ± 0.32	0.46 ± 0.25	0.18 ± 0.12	71%
2CO$_2$_FLOR-FA	101–300	3351	16.7 ± 2.1	0.49 ± 0.31	0.34 ± 0.23	0.15 ± 0.12	68%

northern GoC as a moisture source for the monsoon rainfall in southwestern Arizona (Mitchell et al. 2002; Erfani and Mitchell 2014). There may be several other reasons for this bias, including the inability of parameterized convection to propagate westward (Luong et al. 2018); a weak GoC low-level jet due to unphysical representation of the northernmost part of the GoC; and an oversmoothed topography that might not efficiently block ventilation of drier, more stable air from the Pacific (Bhattacharya et al. 2017).

c. GoC surge analysis

The monsoon (summer) season is here defined as 21 June–30 September. This period is chosen because monsoon onset over the Southwest typically occurs later than 21 June, while the retreat is in late September (Higgins et al. 1997). GoC surges are identified using an empirical orthogonal function (EOF) analysis of the temporal covariance matrix of the summertime "alongshore" GoC near-surface wind anomalies (Bordoni and Stevens 2006). This method has been successfully applied in Pascale and Bordoni (2016) and Pascale et al. (2016) and is briefly described in the appendix. Days between subsequent surges are identified as individual "nonsurge" periods. A mean value of 15 surge events during the 21 June–30 September period is common in both ERA-I and MERRA (Table 2). FLOR slightly underestimates the number of surges per year (14), whereas FLOR-FA slightly overestimates it (16), with both nonetheless being within the observed interannual variability.

To evaluate the impact of GoC surges on the intensity of the associated convection, and assess the models' capability to capture these events, we classify GoC surges based on the intensity of the mean precipitation they are associated with over Arizona (as defined in Fig. 1a). We define the mean precipitation intensity p_{su} for each surge period as $p_{su} \equiv \langle P_{su} \rangle / N_{su}$ and for each nonsurge period as $p_{ns} \equiv \langle P_{ns} \rangle / N_{ns}$. Here $\langle \cdot \rangle$ denotes area averaging over the Arizona domain defined in

Fig. 1a, P_{su} (P_{ns}) is the accumulated rain amount (mm) during surge (nonsurge) days, and N_{su} (N_{ns}) is the number of days of a surge (nonsurge) event. To account for more localized high-impact daily weather events occurring anywhere within the Arizona domain, we also evaluate, for each surge (nonsurge) day, the maximum gridpoint daily precipitation within such domain. This is useful to answer the question of whether the probability of high-impact rainfall events will increase in Arizona and surrounding areas at the gridpoint level under higher levels of atmospheric CO_2.

Anomalies associated with surge conditions are evaluated by building composites of daily anomalies of 10-m wind, total precipitation, and 500-hPa geopotential height and winds for GoC surges associated with (i) $p_{su} < p_{50}$; (ii) $p_{50} \leq p_{su} < p_{95}$; and (iii) $p_{su} \geq p_{95}$ from both reanalyses and model data. We choose p_{95} as a high-percentile threshold that provides a number of events (Table 3) sufficient for statistical significance of the resulting composites. The 95th and 99th percentiles are thresholds commonly chosen for evaluations of precipitation extremes in the NAM region (e.g., Arriaga-Ramírez and Cavazos 2010; Favors and Abatzoglou 2013; Tripathi and Dominguez 2013). The same filtering used prior to the EOF analyses (this section and appendix) is applied to remove the seasonal cycle in all variables

TABLE 3. Values of the 50th, 90th, 95th, and 99th percentile (mm day^{-1}) for surge and nonsurge precipitation (mm day^{-1}) in observed rainfall products (CPC, TRMM), reanalyses (ERA-I, MERRA), and present-day climate model simulations.

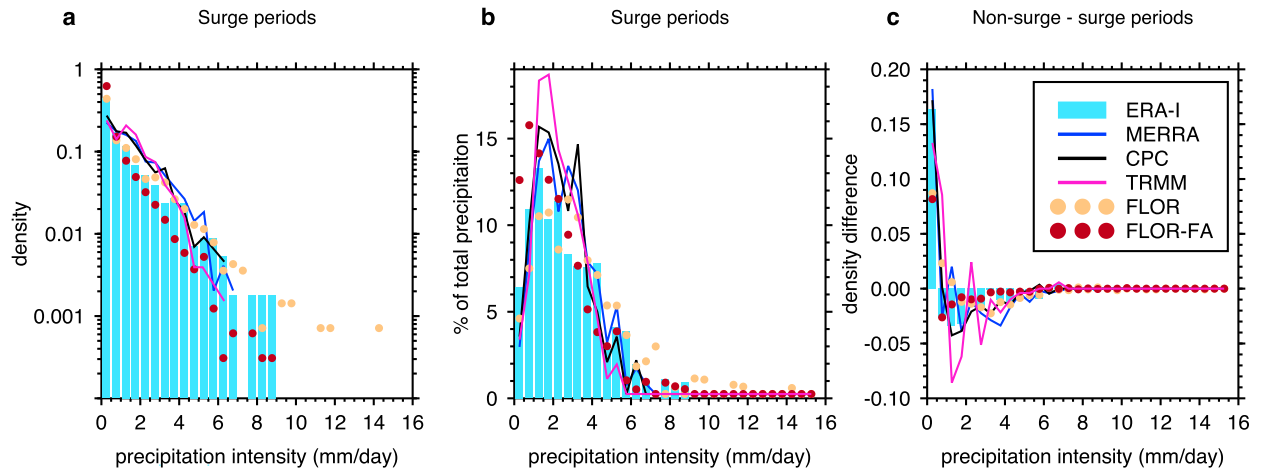| Dataset	Surges				Nonsurges			
	p_{50}	p_{90}	p_{95}	p_{99}	p_{50}	p_{90}	p_{95}	p_{99}
CPC	1.0	3.2	3.8	5.0	0.6	2.7	3.2	5.0
TRMM	1.3	3.0	3.5	4.4	0.7	2.4	2.9	4.2
ERA	0.6	3.0	4.2	6.0	0.5	2.2	3.4	5.2
MERRA	1.2	3.5	4.4	5.3	0.8	2.5	3.0	4.6
FLOR	0.7	3.4	4.5	6.9	0.4	2.2	3.4	6.3
FLOR-FA	0.4	1.9	2.8	4.8	0.2	1.5	2.2	4.0

FIG. 2. (a) Histograms (bin: $0.5\,\mathrm{mm\,day}^{-1}$) of precipitation distribution in ERA-I (bars), MERRA (blue), CPC (black), TRMM (magenta), and model data (scattered dots); (b) percentage contribution within each bin to the total surge precipitation P_{su} (%); (c) difference between nonsurge and surge histograms of precipitation distribution.

(see appendix), so all statistics are computed for anomalies relative to the summertime climatology. Finally, near-surface winds and humidities, and the midtropospheric large-scale environment during surge and nonsurge days are analyzed through composites of daily means of 10-m moisture fluxes $(qu, qv)_{10m}$, specific humidity q_{10m}, saturation specific humidity $q^*_{10m}(T, p)$, and 500-hPa geopotential height. The saturation specific humidity is calculated as $q^* \approx 0.622e^*/\pi$, with π being the pressure in hPa and e^* being saturated vapor pressure given by the August–Roche–Magnus formula $e^* = 6.112 \exp[17.62T/(243.12 + T)]$ (WMO 2008).

3. Model evaluation of high-intensity precipitation events

In the following, we evaluate the model's capability of reproducing both the statistics of GoC moisture surges and associated precipitation and the large-scale patterns associated with precipitation events of different intensity.

a. Precipitation during surge and nonsurge periods

The frequency distribution of surge-related mean precipitation intensity for CPC, TRMM, ERA-I, MERRA, FLOR, and FLOR-FA is shown in Fig. 2a. Values of p_{50}, p_{90}, p_{95}, and p_{99} (p_X denotes the Xth percentile of p) are reported[5] in Table 3. Although quite frequent,

surges associated with $p_{su} < p_{50}$ only modestly contribute to P_{su} ($\approx$5%) over Arizona (Fig. 2b). GoC surges associated with $p_{50} \leq p_{su} < p_{95}$ provide the largest contribution to P_{su} ($\approx$70%–75%). While rare (5% of the total), GoC surges associated with very intense regional precipitation events (e.g., $p_{su} \geq p_{95}$) explain a nonnegligible fraction of total surge-related precipitation ($\sim$20%). In ERA-I, GoC surges tend to be drier than in MERRA and CPC ($p_{50} = 0.6\,\mathrm{mm\,day}^{-1}$ vs $1.2\,\mathrm{mm\,day}^{-1}$), but tend to generate more high-impact rainfall events (e.g., $p_{99} = 6$ vs $5\,\mathrm{mm\,day}^{-1}$). Overall, FLOR compares well with observations and reanalyses, although it overestimates the probability of the most intense rainfall events. Reduction of SST biases through flux adjustment (FLOR-FA) increases (decreases) the number of surges featuring low (high) rainfall percentiles, overall reducing the mean NAM precipitation.

During GoC surges, on average, convective rainfall tends to be more intense compared to that occurring during nonsurge days, as evident from the percentile values in Table 3 and the difference between the nonsurge and surge histograms of the precipitation distribution in Fig. 2c. Both reanalyses and observations show that intermediate and heavy rainfall (i.e., $p > 0.5\,\mathrm{mm\,day}^{-1}$) is $\sim$20% less frequent during nonsurge days as compared to surge days. Our findings show that widespread rainfall events are on average more intense during GoC surge periods than during nonsurge periods, providing support to earlier work (e.g., Favors and Abatzoglou 2013). Overall, FLOR in both configurations behaves fairly consistently with reanalyses and observations in characterizing surge versus nonsurge precipitation.

---

[5] In p we omit the subscripts "su" and "ns" to simplify the notation when it is obvious from the context if we are referring to surge or nonsurge precipitation.
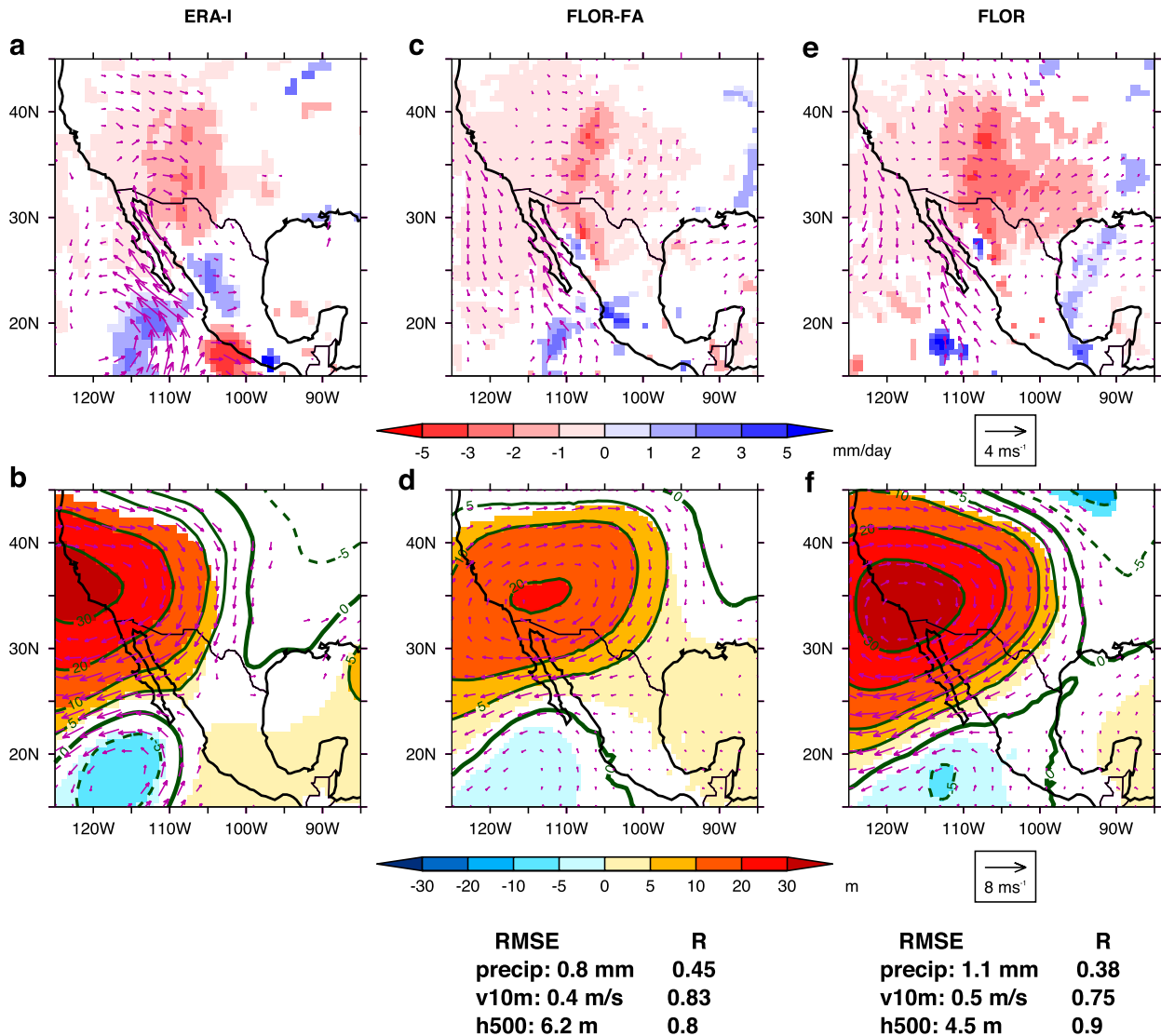
FIG. 3. Composites of (a),(c),(e) precipitation (color shading) and 10-m wind anomalies (arrows) and (b),(d),(f) 500-hPa geopotential height (color shading and green contours) and wind (arrows) anomalies the day after the onset (day 1) of a GoC surge with mean precipitation intensity $p_{su} < p_{50}$. Color shading and wind anomalies are shown only where composites are statistically significant at the 5% level according to a two-tailed t test. Composites are shown for (a),(b) ERA-I; (c),(d) FLOR-FA; and (e),(f) FLOR. RMSE, and linear correlation R relative to (a),(b) and estimated over the domain in the figure are reported for composite fields.

b. Spatial circulation patterns

Composites for GoC surges associated with low rainfall intensity are shown in Fig. 3 for ERA-I (Figs. 3a,b), FLOR-FA (Figs. 3c,d), and FLOR (Figs. 3e,f) for day +1 (i.e., the second surge day), which is the day when the heaviest precipitation tends to occur. In spite of a strong anomalous southeasterly flow along the GoC, negative precipitation anomalies especially over Arizona indicate below-average rainfall. As discussed in previous studies (e.g., Higgins et al. 2004; Schiffer and Nesbitt 2012), the presence of an anticyclonic anomaly

at 500 hPa centered over Southern California shifts the monsoonal ridge westward and induces an anomalous midtropospheric northerly flow into the Southwest, which brings in drier, more stable midtropospheric air. Both FLOR-FA (Fig. 3d) and FLOR (Fig. 3f) capture the pattern of anomalous 500-hPa geopotential height, although they both feature a generally weaker tropical disturbance south of the GoC (Pascale et al. 2016). Similar patterns are seen in MERRA (see Fig. S1 in the online supplemental material).

GoC surges associated with $p_{50} \leq p_{su} < p_{95}$ (Fig. 4a) are characterized by positive precipitation anomalies
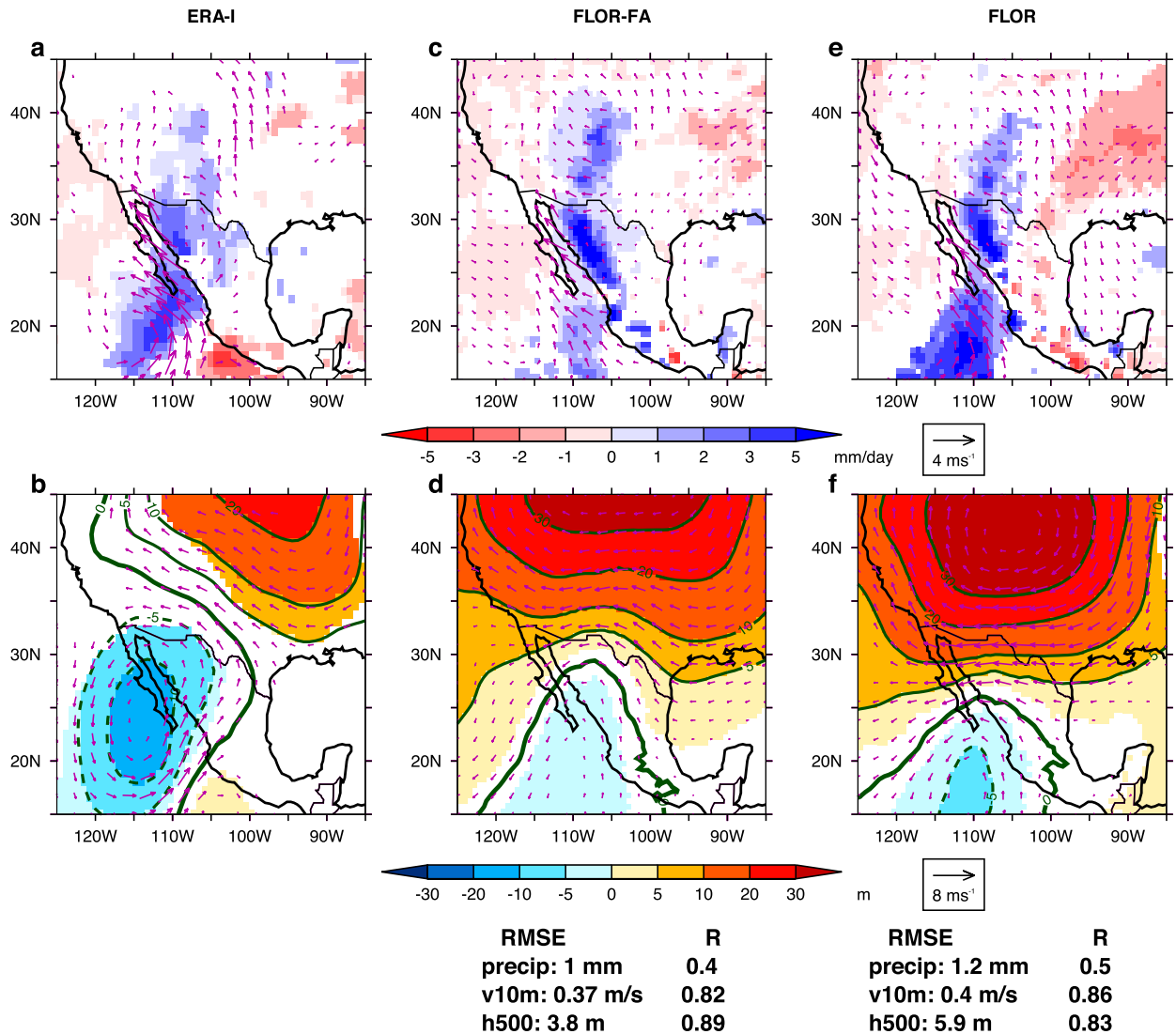
FIG. 4. As in Fig. 3, but for $p_{50} \leq p_{su} < p_{95}$. RMSE and linear correlation R relative to (a),(b) and estimated over the domain in the figure are reported for composite fields.

over most of Arizona and surrounding regions (Fig. 4a), which tend to persist for three to five days. These events differ from those associated with lower-intensity rainfall (Fig. 3) mainly in the position of the midtropospheric anticyclonic anomaly, which is centered northeast of New Mexico. This results in a northeastward displaced midtroposphere monsoonal ridge and, consequently, an anomalous easterly–southeasterly flow into the monsoon region. The cyclonic anomaly to the south of the GoC (Fig. 4b) is meridionally elongated from 15° to 30°N, and thus is compatible with either a tropical disturbance (e.g., a tropical storm/cyclone or a tropical easterly wave, both of which can trigger a GoC surge) or an upper-level inverted trough occurring simultaneously with a GoC surge (e.g., Seastrand et al. 2015).

Both models underestimate the tropical cyclonic anomaly and do not fully capture its northernmost extent (Figs. 4b,d,f). In FLOR, this bias is likely to be attributed to the erroneous southward displacement of the climatological monsoon high, induced by the model SST biases (Pascale et al. 2016), which disfavor the entrance of upper-level inverted troughs into the region from the Gulf of Mexico (e.g., Bieda et al. 2009; Finch and Johnson 2010).

GoC surges associated with $p_{su} \geq p_{95}$ (Fig. 5) are characterized by a midtropospheric cyclonic anomaly located over the northern GoC (Fig. 5b), and an anticyclonic anomaly over the central United States displaced to the east of the Four Corners region (Fig. 1a) and elongated southward over Texas and the Gulf of
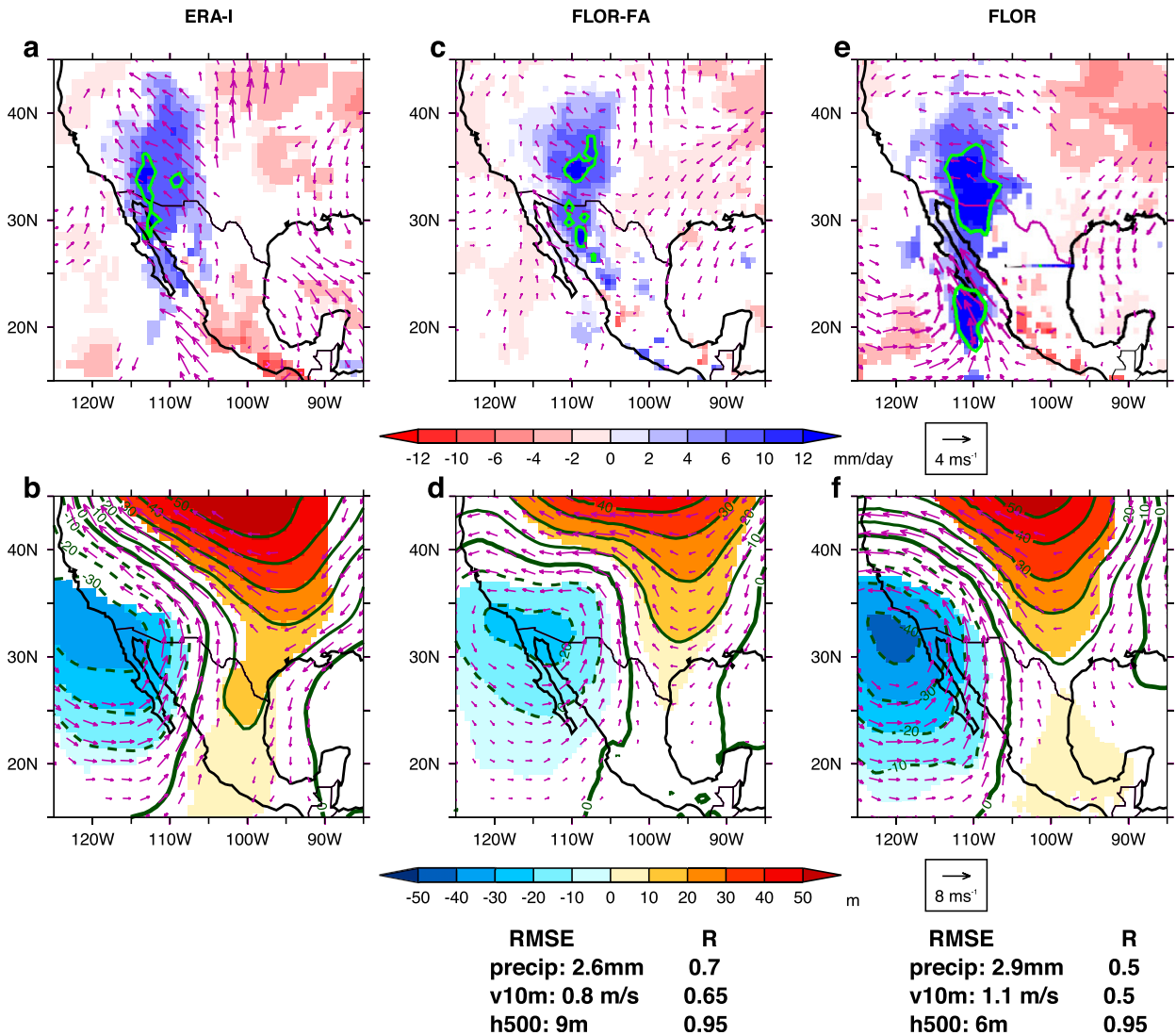
FIG. 5. As in Fig. 4, but for $p_{su} \geq p_{95}$. Green contours in (a),(c),(d) denote regions where precipitation anomalies exceed 8 mm day^{-1}. RMSE and linear correlation R relative to (a),(b) and estimated over the domain in the figure are reported for composite fields.

Mexico. These features are consistent with severe weather event patterns identified in previous studies (Maddox et al. 1995; Favors and Abatzoglou 2013; Mazon et al. 2016). Interestingly, reanalyses and FLOR-FA (Figs. 5a,c) show no cyclonic anomaly to the south of the GoC, suggesting that in Arizona intense and widespread events are primarily determined by synoptic variability associated with midlatitude Rossby waves (e.g., Pascale and Bordoni 2016). Contrary to reanalyses, composites of extreme surge precipitation in FLOR show evidence of a strong lower-level cyclonic anomaly to the southwest of the GoC associated with tropical cyclones (TCs; Fig. 5e). An excessive TC activity in the eastern North Pacific, and more generally in the whole

North Pacific, is a common bias in FLOR and is tightly linked to SST biases [Fig. 5 in Vecchi et al. (2014)]. Reduction of SST biases in FLOR-FA improves TC activity in the eastern North Pacific, resulting in composites of extreme surge precipitation events more in line with those from reanalyses (Fig. 5c; supplemental Fig. S3). At 500 hPa, FLOR-FA also better positions the anticyclonic anomaly over the Gulf of Mexico and the cyclonic anomaly over the GoC (Figs. 5b,d,f).

4. Influence of CO_2 forcing on GoC surges

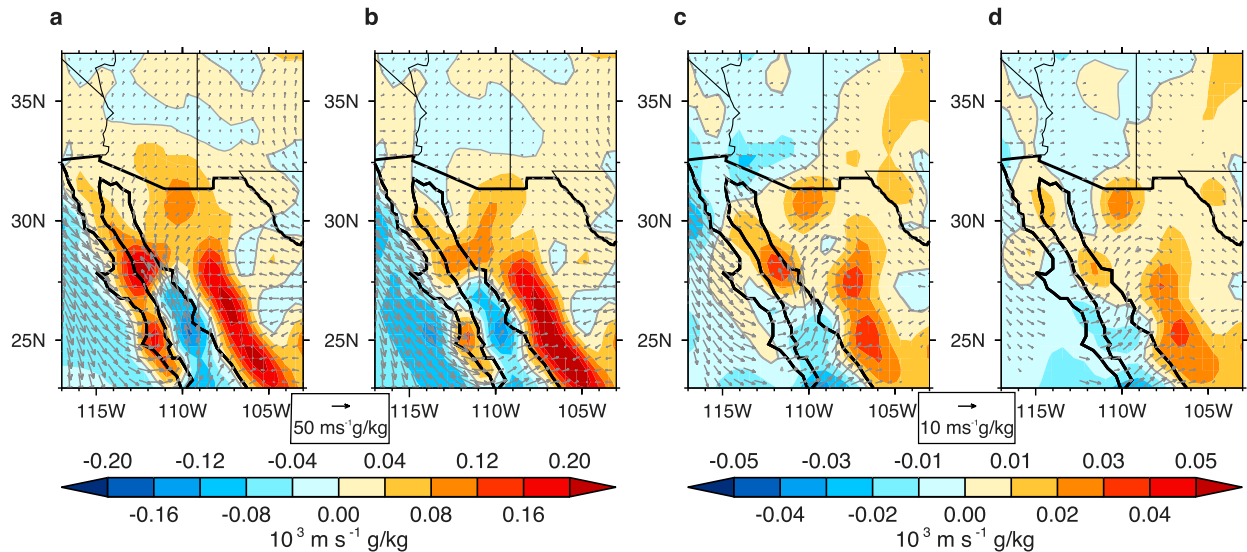As shown in Figs. 3, 4, and 5, for each precipitation category, FLOR-FA shows a better agreement with

FIG. 6. Composites (CTRL_FLOR-FA) of 10-m moisture flux, $(q\mathbf{u})_{10m}$ (gray arrows), and 10-m moisture flux convergence (color shading), $-\nabla \cdot (q\mathbf{u}_{10m})$, for (a) surge days and (b) nonsurge days. Mean change (2CO_2_FLOR-FA minus CTRL_FLOR-FA) in the 10-m moisture flux (gray arrows) and 10-m moisture flux convergence (color shading) for (c) surge days and (d) nonsurge days. In (c) and (d), arrows are shown only where the differences are statistically significant at the 95% level on the basis of a t test.

reanalyses in terms of RMSE and spatial correlations 13 out of 18 times as compared to FLOR. In section 2b, we have further discussed the improvements that flux adjustment brings to precipitation climatology over North America [see also Pascale et al. (2017)]. This gives us confidence to use FLOR-FA to extend our analysis to the impacts of warming induced by CO_2 doubling on GoC surges.

a. Impact on low-level moisture

During surge days, southeasterly near-surface (10 m) moisture fluxes are stronger over the GoC as compared to nonsurge days, with a stronger convergence especially over northwestern Mexico and Arizona (CTRL_FLOR-FA; Fig. 6a). In the 2CO_2 _FLOR-FA run, moisture fluxes weaken in the northern GoC and acquire a larger southwesterly component in the rest of the GoC, likely to be associated with the increase in the land–sea contrast. Consistently, convergence of surge near-surface moisture fluxes is reduced over Arizona and increased over northwestern Mexico (Fig. 6c). During nonsurge days (Fig. 6b), similar changes are projected by FLOR-FA, although there is smaller reduction in moisture convergence over Arizona (Fig. 6d). The response pattern shown in Fig. 6 over the northern GoC (i.e., north of 28°N) may be affected by the fact that the model configuration places land grid points where the sea extends in reality. Given a more realistic representation of the GoC, we might conjecture that the pattern of positive convergence as well as the pattern of positive convergence change within the GoC at

about 28°N (Fig. 6a) might have been located at the northern end of the GoC (Fig. 6c).

It is important to note that increases in near-surface moisture flux convergence and in near-surface specific humidity over land do not necessarily imply more vigorous deep convection. In fact, since continental lands warm more than oceans, increases in near-surface specific humidity q_{10m} due to moisture transport from oceans to land may not keep pace with the rise in saturation specific humidity $q^*_{10m}(T, p)$ (e.g., Byrne and O'Gorman 2018). In the NAM region, this may imply a more unsaturated boundary layer and lower probability for rising parcels to overcome entrainment of dry midtropospheric air (Adams and Souza 2009), preventing the development of deep convection. During surge days, q_{10m} generally increases between 4% and 10% over Arizona and New Mexico (Fig. 7a) while temperature rises between 6% and 18% (Fig. 7b). As a result, $q^*_{10m} - q_{10m}$ increases by approximately 15%–30%, leading to a more unsaturated low-level environment, especially over the elevated terrains, where, therefore, the most substantial surge-rain reductions are expected to occur (Fig. 8). During nonsurge days, relative increases in q_{10m} are larger than during surge days, partially offsetting temperature increases and leading to a more modest increase in $q^*_{10m} - q_{10m}$ (Figs. 7d–f).

b. Impact on precipitation

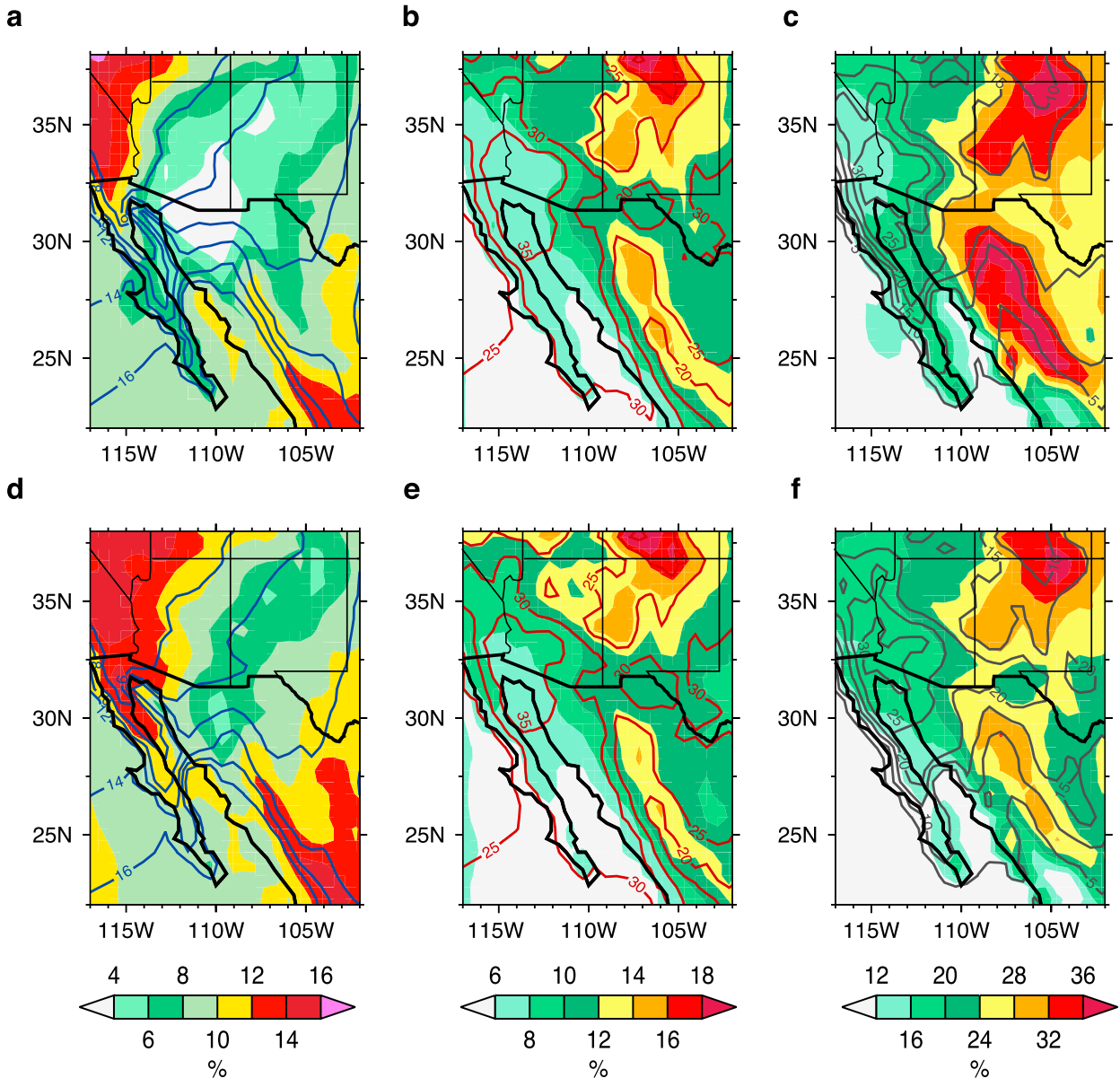Consistent with the pattern of changes of low-level saturation reductions shown in Fig. 7c, a decrease of

FIG. 7. Percentage change (color shading; %) of (a) 10-m specific humidity q_{10m}, (b) 10-m temperature T_{10m}, and (c) $q^*_{10m} - q_{10m}$ for the surge-day composites. CTRL_FLOR-FA values are denoted by blue contours (g kg^{-1}), red contours (°C), and gray contours (g kg^{-1}) for q^*_{10m}, 10-m temperature, and $q^*_{10m} - q_{10m}$, respectively. (d)–(f) As in (a)–(c), but for the nonsurge day composites.

summertime precipitation is projected by FLOR-FA during surge days (Fig. 8a). Nonsurge rainfall is also projected to decline, with a pattern consistent with that of the changes in $q^*_{10m} - q_{10m}$ (Fig. 7f), although reductions are less significant, particularly over Arizona (Fig. 8b). In spite of the substantial reduction of summertime precipitation (Fig. 9a), an increase in precipitable water is projected in FLOR-FA, especially to the north of the GoC, as a result of CO_2 doubling and the consequent rise of mean surface

temperature (Fig. 9b). Luong et al. (2017) show that over the last half a century summertime precipitable water has on average increased, particularly over southwestern Arizona and southeastern California, and they relate this to the observed more extreme character of NAM precipitation. If we compare the distributions of daily precipitation peaks occurring anywhere within the Arizona domain during all surge days for 1990 with doubled CO_2 levels, there is a clear indication of more frequent events above the 99.9th percentile (Fig. 10a).

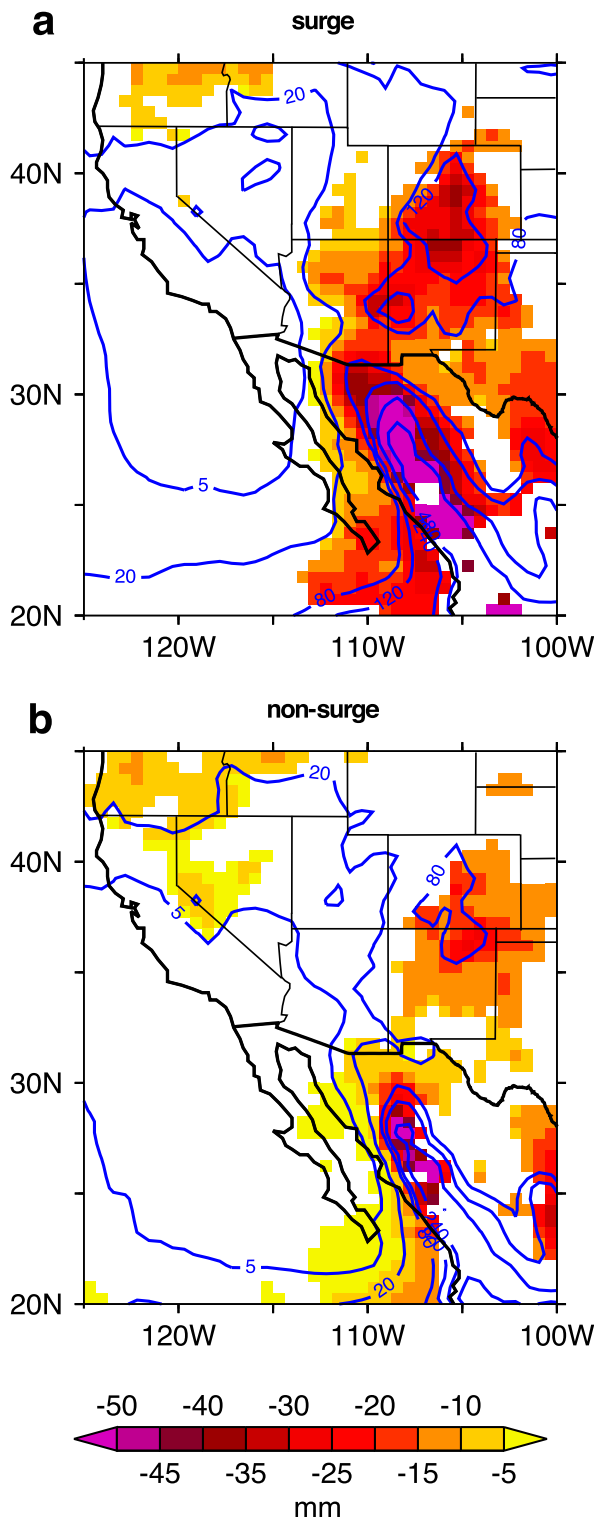FIG. 8. Mean change in accumulated precipitation ($2CO_2$_ FLOR-FA minus CTRL_FLOR-FA) during (a) surge and (b) nonsurge days occurring between 21 Jun and 30 Sep. Blue contours denote the mean CTRL_FLOR-FA accumulated values over the same period. Differences are shown only where statistically significant at the 95% level on the basis of a t test.

Changes in the histograms are statistically significant as per a two-sample Kolmogorov–Smirnov test at the 0.1% level. This suggests that, regardless of where they take place, localized intense rainfall events may become more frequent in the Arizona domain during surge days. Furthermore, Fig. 10a also shows a reduction in the frequency of intermediate-to-high intensity surge events, consistent with the substantial and statistically significant precipitation decrease shown in Fig. 8a. Similarly, localized nonsurge convective rainfall is projected to become less intense, that is, more frequent at low-intensity values and less frequent at intermediate-to-high intensity values (Fig. 10b). Unlike surge rains, there is no evidence from Fig. 10b that localized, high-intensity nonsurge convective rainfall will become more frequent under CO_2 doubling.

A more detailed regional view of the potential impact of CO_2 forcing on surge and nonsurge precipitation events of different intensity is provided in Fig. 11 with a quantification of the statistical significance. Surge rains that are more strongly affected by CO_2 forcing are those of intermediate-to-high intensity ($p_{50} \leq p < p_{99}$; Fig. 11c). Precipitation events within this category are expected to experience substantial and significant reductions over most of the North American Southwest. Reductions of surge rain at $p_{su} < p_{50}$ are significant over the Sonoran Desert and southern Arizona, but statistically insignificant elsewhere (Fig. 11a). At the high end, Fig. 11e suggests that most of the changes in rainfall totals from extreme surge rains ($p \geq p_{99}$) are broadly statistically insignificant, except for limited areas in western Arizona and to the north of the GoC. The precipitation response seen during nonsurge days is fairly consistent with that during surge days, although projected changes are less statistically significant for most percentiles ($p_{ns} < p_{99}$; Figs. 11b,d). In particular, at the highest percentiles ($p \geq p_{99}$), nonsurge rainfall decreases in response to CO_2 forcing (Fig. 11f), especially over elevated terrains in Arizona (i.e., Mogollon Rim) and northwestern Mexico (i.e., Sierra Madre Occidental).

c. Impact on the large-scale midtropospheric flow

As discussed in section 3, the position and strength of the monsoonal ridge is a primary large-scale control on the intensity and spatial extent of NAM precipitation. We therefore explore how possible changes in the monsoonal ridge due to greenhouse gas forcing are related to precipitation changes discussed in the previous subsection. Summertime changes in the mean 500-hPa geopotential height in $2CO_2$ _FLOR-FA relative to
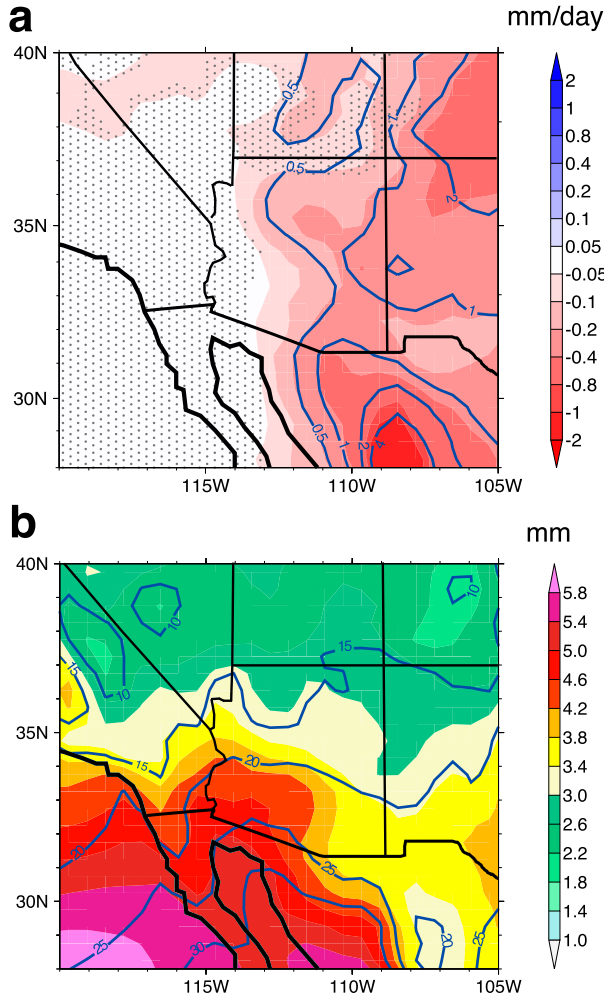
FIG. 9. (a) Precipitation mean (21 Jun–30 Sep) change induced by CO_2 doubling in FLOR-FA. Stippling indicates regions where precipitation differences are not statistically significant at the 5% level on the basis of a t test. (b) Precipitable water mean change for the same period. Blue contours denote the climatological values for precipitation (mm day^{-1}) and precipitable water (mm) in (a) and (b), respectively.

FIG. 10. Change (2CO$_2$_FLOR-FA minus CTRL_FLOR-FA) in the distribution of maximum daily precipitation within the Arizona domain (Fig. 1a) during (a) surge and (b) nonsurge days. The insets in (a) and (b) zoom over values larger than 99.9th percentile in the control run ($\approx$60 mm day^{-1}).

CTRL_FLOR-FA are shown in Fig. 12. As expected, in response to CO_2 doubling, the 500-hPa geopotential height generally rises, owing to the warming and thermal expansion of the lower-to-middle troposphere (e.g., Christidis and Stott 2015). To the first order, this causes an expansion of the ridge. An expansion of the monsoonal ridge has been associated by Lahmers et al. (2016) with a southward displacement of the upper-level inverted troughs and thus with a reduced role of these disturbances in the initiation and organization of monsoon convection over Arizona. To a second order, the positive 500-hPa geopotential height anomalies are not spatially uniform, but tend to be larger on the west side of the monsoonal ridge (Fig. 12). A consequence
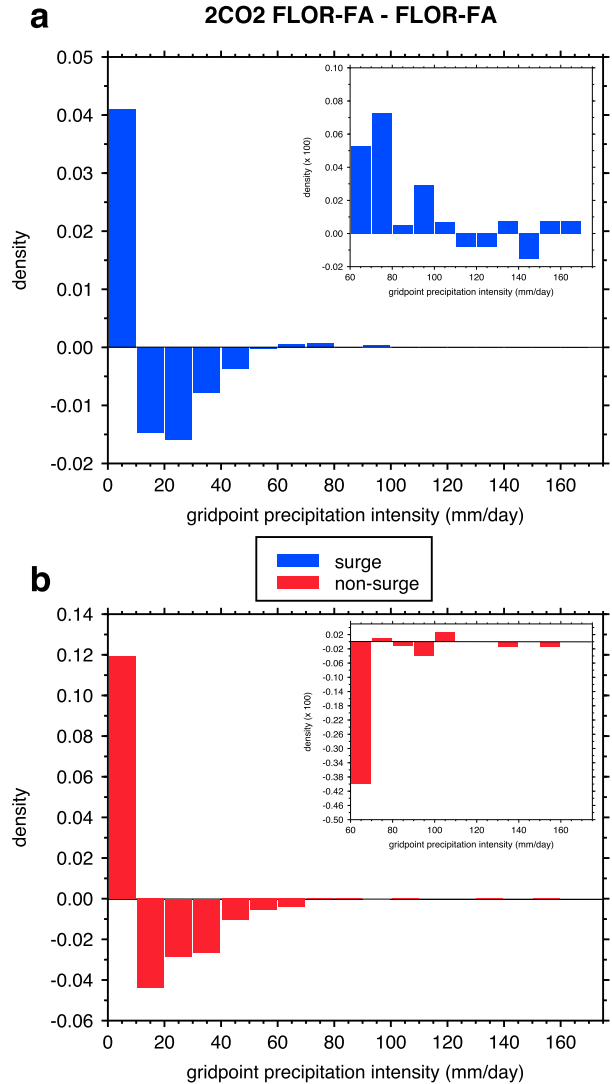
of the pattern shown in Fig. 12 is a westward shift in the climatological position of the monsoonal ridge. This westward displacement might support stronger subsidence over western Arizona, an anomalous northerly flow over northwestern Mexico that could further divert southward upper-level inverted troughs, and an overall drier NAM (Fig. 11). Composites of 500-hPa geopotential height for surge/nonsurge days (Fig. 13) further detail changes in the midtroposphere during low, medium, and high precipitation events. During GoC surge events featuring $p_{su} < p_{50}$, 500-hPa geopotential height anomalies are collocated with the 500-hPa geopotential height itself (Fig. 13a), implying an intensification of
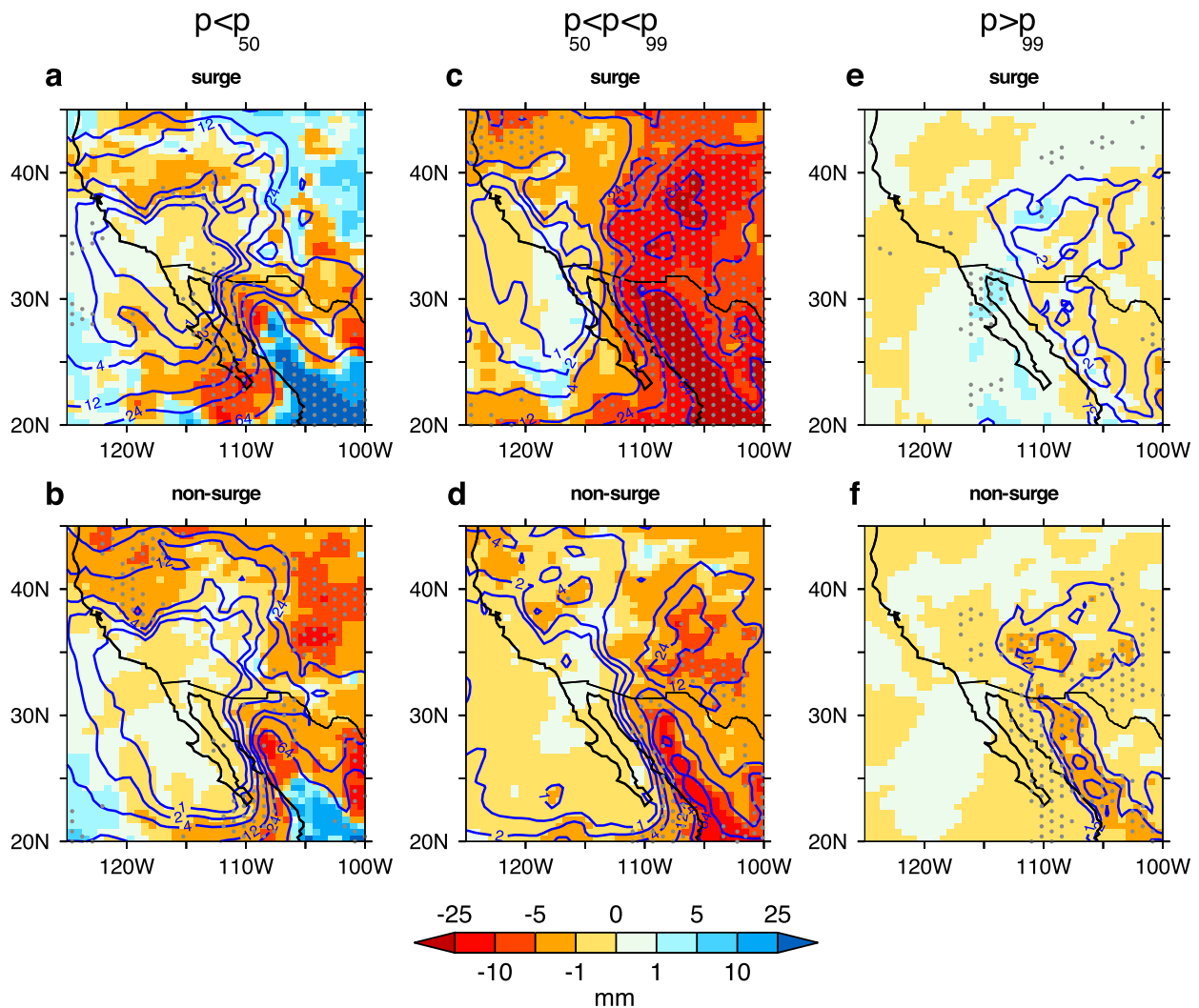
FIG. 11. Mean change (2CO$_2$_FLOR-FA minus CTRL_FLOR-FA) in accumulated precipitation during (top) surge and (bottom) nonsurge days between 21 Jun and 30 Sep for (a),(b) low precipitation intensity ($p < p_{50}$); (c),(d) intermediate-to-high precipitation ($p_{50} < p < p_{99}$); and (e),(f) extreme precipitation intensity ($p > p_{99}$). Blue contours denote the mean CTRL_FLOR-FA values, and stippling indicates regions where differences are statistically significant at the 95% level on the basis of a t test.

the monsoonal ridge and hence stronger subsidence, consistent with precipitation reductions therein (Fig. 11a). Changes in the monsoonal ridge during GoC surge events featuring $p_{50} < p_{su} < p_{99}$ are characterized by a local minimum of 500-hPa geopotential height anomalies collocated with the monsoonal ridge (Fig. 13b) and the consequent weakening of the southeasterly mid-tropospheric flow around its southern flank (black arrows in Fig. 13b). As this southeasterly flow is crucial for advecting moisture from the Gulf of Mexico into the Southwest, the change in 500-hPa geopotential height is consistent with the reduction in precipitation shown in Fig. 11. Figure 13c shows no statistically significant changes in 500-hPa geopotential height over the western

United States, which may imply that anomalies in surge rains at $p_{su} > p_{99}$ seen in Fig. 11e are not attributable to dynamically driven changes in the midtropospheric flow, but instead arise solely because of increased precipitable water. During nonsurge precipitation events, 500-hPa geopotential height anomalies (Figs. 13b,d,f) generally feature a ridging over the western United States, similar to the mean summertime 500-hPa geopotential height anomalies shown in Fig. 12.

5. Discussion

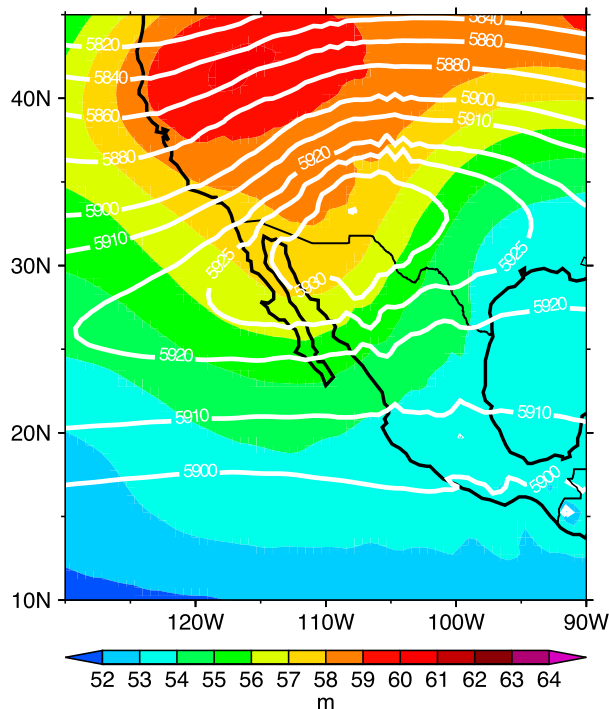Under CO$_2$ doubling, both FLOR and FLOR-FA suggest no significant changes in the mean number of

FIG. 12. Mean summertime (21 Jun–30 Sep) difference in 500-hPa geopotential height (CTRL_FLOR-FA vs 2CO₂_FLOR-FA; shaded contours). White contours denote mean CTRL_FLOR-FA values in meters.

GoC moisture surges per year (Table 2). The main triggers of GoC surges are tropical easterly waves and TCs passing to the south of the GoC (e.g., Fuller and Stensrud 2000). Recent studies show that the preferred track of TCs (e.g., Bengtsson et al. 2006; Murakami et al. 2012) and tropical easterly waves (e.g., Serra and Geil 2017) over Central America and the eastern Pacific may shift southward in future high-emission projections. In principle, everything else being held equal, a southward shift of these easterly disturbances could reduce the number of GoC surges, and thus directly impact rainfall patterns over Arizona. Analyses of the 850-hPa high-passed (2–6 days) meridional wind in present-day and CO_2 doubling conditions reveal a minimal southward shift in the tropical easterly wave track in both FLOR and FLOR-FA (not shown). Comparison of sea level pressure and 850-hPa geopotential composites (not shown) suggests that in 2CO₂_FLOR-FA there is no significant southward shift of the cyclonic anomaly associated with GoC surges [e.g., Fig. 5 of Pascale et al. (2016)], consistent with no changes in their mean number.

Although our numerical experiments show that the total number of GoC surges is not significantly affected by CO_2 doubling, changes in the mean atmospheric background environment are likely to impact the initiation and the intensity of convective activity during surge days. Low-level moisture fluxes associated with GoC surges as well as their convergence over land to the east of the GoC (Fig. 6) are projected to intensify as a result of a warmer atmosphere. The low-level moisture increases, however, are not matched by the larger increments in the near-surface saturation specific humidity, dictated by amplified land warming (e.g., Byrne and O'Gorman 2018), and thus make GoC surges more ineffective in saturating near-surface air. These conclusions further support the results in Pascale et al. (2017), who showed that, under CO_2 doubling, increased mean lower-atmospheric stability is associated with a reduction of the NAM rainfall. Besides these thermodynamic changes, here we further document that nonuniform changes in the mean midtropospheric geopotential height result in an expansion and westward displacement of the monsoonal ridge (Fig. 12) and, during GoC surges, in a weakened southeasterly flow along its southern flank (Figs. 13c,d). Stronger ridging over the western United States is projected also by CMIP5 models (e.g., Maloney et al. 2014) and is expected to reduce synoptic variability over the western United States, thus favoring the conditions for more persistent anticyclones (Brewer and Mass 2016). In spite of the more unfavorable atmospheric background, which may reduce the mean surge precipitation (Fig. 8) and shift the mean intensity of surge rainfall toward lower percentiles, we do find that the intensity of localized precipitation within the Arizona domain (Fig. 1a) is projected to increase (Fig. 10a). The increase in the frequency of localized high-intensity precipitation (Fig. 10a) is consistent with the projected increase in precipitable water (Fig. 9b). Projections in mean precipitation, precipitable water, and precipitation extremes in FLOR-FA are consistent with trends that have been observed over the last six decades in western Arizona (Chang et al. 2015; Luong et al. 2017).

A caveat worth mentioning is that extreme precipitation changes are generally underestimated in FLOR as compared to its 25-km counterpart (van der Wiel et al. 2016); thus, here we may be underestimating changes for GoC surges leading to extreme precipitation. Additional clarifications to our results that need to be emphasized are (i) we have not tried to investigate short-term (i.e., hourly) precipitation extremes during GoC surges, for which convection-permitting models would be necessary; (ii) FLOR underestimates the local evaporative contribution of the northern GoC (missing these factors, we may be underestimating the moisture supply to these regions and, possibly, the magnitude of precipitation extremes; e.g., Schmitz and Mullen 1996; Berbery 2001; Mitchell et al. 2002; Erfani and Mitchell 2014); and (iii) upper-level inverted troughs (e.g., Bieda et al. 2009; Finch and Johnson 2010; Lahmers et al. 2016), which are
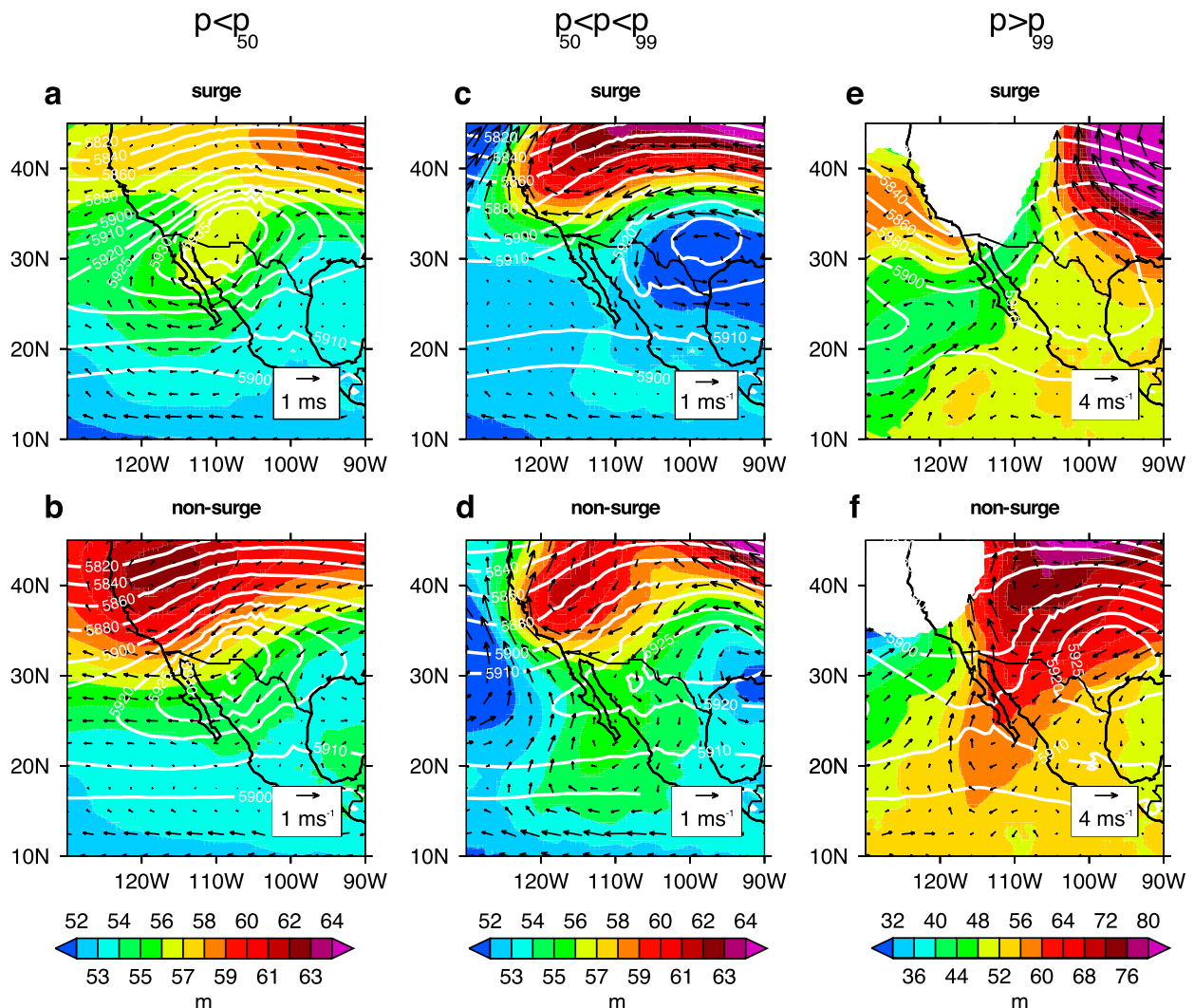
FIG. 13. Mean 500-hPa geopotential height (color shading) and wind (vectors) change (2CO$_2$_FLOR-FA minus CTRL_FLOR-FA) during (top) surge and (bottom) nonsurge days between 21 Jun and 30 Sep for (a),(b) low precipitation intensity ($p < p_{50}$); (c), (d) intermediate-to-high precipitation ($p_{50} < p < p_{99}$); and (e),(f) extreme precipitation intensity ($p > p_{99}$). White contours denote the mean CTRL_FLOR-FA values. Differences are shown only where they are statistically significant at the 95% level on the basis of a t test (only affects $p > p_{99}$).

another important synoptic forcing in addition to gulf surges, have not been included in this study. However, we do find that GoC surges leading to the heaviest and most widespread precipitation are those occurring simultaneously with the passage of an upper-level inverted trough over the northern NAM region (Fig. 5).

6. Conclusions

Using FLOR-FA, a 50-km horizontal resolution GCM, we have shown that the mean number of GoC surge events per monsoon season does not change under CO_2 doubling. Nevertheless, our simulations indicate that the monsoonal rainfall will be reduced over Arizona

because surge-related intermediate-to-high intensity precipitation will be reduced. We further show that these changes are associated with (i) a decrease in the relative humidity of near-surface air due to amplified land warming (Figs. 6 and 7), which decreases the probability for rising parcels to overcome the entrainment of dry midtropospheric air (Adams and Souza 2009), thus inhibiting deep convection, and (ii) a nonuniform expansion of the monsoonal ridge, which weakens the easterly flow along the southern flank of the monsoonal ridge (Fig. 13c), reducing easterly wind shear (e.g., Bieda et al. 2009; Newman and Johnson 2012) and moisture transport from the Gulf of Mexico, thus favoring a more stable atmosphere (Pascale et al. 2017). The distribution of daily precipitation peaks

occurring anywhere within the Arizona domain shifts toward more extreme values for values larger than the 99.9th percentile, consistent with precipitable water changes. Additionally, convective rainfall not occurring during surge days is also expected to decrease but with no significant changes for the most intense rainfall events.

What our study suggests for Arizona and the surrounding areas is a more arid summer, but with the possibility of more high-impact precipitation events. Given the more arid conditions, extreme rainfall may be even more damaging because of the higher impermeability of dry land. As a consequence, improved adaptation measures might be required to cope with the projected reduced and more extreme monsoon rainfall due to higher levels of greenhouse gas concentrations. While the conclusions reached in this study are based on a single GCM, this GCM (FLOR) has been the first one to be shown to realistically represent GoC surges (Pascale et al. 2016). As increasing horizontal resolution in state-of-the-art GCMs will soon reach 50 km or higher, new comparative, process-based studies will be possible and allow for a better quantification of the uncertainty associated with the NAM response to global warming. Furthermore, efforts are underway at NOAA/ GFDL to develop high-resolution stretched global grid modeling (Harris et al. 2016) and to integrate two-way nested convection-permitting models into global models used for seasonal and decadal prediction (Harris and Lin 2014). Hence, focus on short-term (i.e., hourly) precipitation extremes occurring during the NAM season will soon be pursued in future studies.

APPENDIX

Surge Identification Algorithm

To identify "surge" and "nonsurge" periods, we determine the leading standardized principal components (PCs) through an EOF analysis of the temporal covariance matrix of the summertime "alongshore" GoC near-surface wind anomalies. This is defined as the component of the 10-m wind anomaly over the GoC parallel to its axis (Fig. 1). Wind anomalies, as well as anomalies of all other variables analyzed in this paper, are obtained by applying a Lanczos high-pass filter (Duchon 1979) with a cutoff frequency of 100 days (e.g., Kikuchi and Wang 2009) and by removing the mean and linear trends from the time series for the period 21 June–30 September.

PC1 is highly correlated with the domain-averaged alongshore wind anomalies, and EOF1 corresponds to a mode with strong, northward near-surface wind anomalies over the whole GoC; PC2 is highly correlated with the difference between the northern and southern domain-averaged alongshore wind anomalies, and EOF2 describes a mode with northward and southward alongshore near-surface wind anomalies in the northern and southern GoC, respectively. As explained in Pascale and Bordoni (2016), in most cases a large PC1 peak is followed by a large PC2 peak, a sequence that describes the life cycle (northward propagation) of a major surge. Less frequently, peaks in PC2 occur without corresponding peaks in PC1: these represent more localized GoC surges (minor surges, e.g., Adams and Comrie 1997) originating in the middle of the GoC and are often associated with upper-level inverted troughs (Bieda et al. 2009; Finch and Johnson 2010).

"Surge" periods are identified by determining the days for which *either* PC1 *or* PC2 is above 0.75 (i.e., 75% of its standard deviation). The last day of a surge event and the onset of a successive one have to be separated by at least one nonsurge day, for which PC1 *and* PC2 are both less than 0.75. This approach is able to capture both major and minor surge events, which differ in their spatial extent along the GoC. While the 0.75 threshold is somewhat arbitrary, results with slightly different threshold values are not substantially different. It is only for large threshold values (e.g., 1.5) that results differ substantially, with a sharp decrease in the number of identified surges (Pascale and Bordoni 2016).

REFERENCES

Adams, D. K., and A. C. Comrie, 1997: The North American monsoon. *Bull. Amer. Meteor. Soc.*, **78**, 2197–2213, https:// doi.org/10.1175/1520-0477(1997)078<2197:TNAM>2.0.CO;2.

——, and E. P. Souza, 2009: CAPE and convective events in the Southwest during the North American monsoon. *Mon. Wea. Rev.*, **137**, 83–98, https://doi.org/10.1175/ 2008MWR2502.1.

Arriaga-Ramírez, S., and T. Cavazos, 2010: Regional trends of daily precipitation indices in northwest Mexico and southwest United States. *J. Geophys. Res.*, **115**, D14111, https://doi.org/ 10.1029/2009JD013248.

Balling, R. C., 1987: Diurnal variations in Arizona monsoon precipitation frequencies. *Mon. Wea. Rev.*, **115**, 342–346, https://doi.org/10.1175/1520-0493(1987)115<0342:DVIAMP>2.0.CO;2.

Becker, E. J., and E. H. Berbery, 2008: The diurnal cycle of precipitation over the North America monsoon region during the NAME 2004 field campaign. *J. Climate*, **21**, 771–787, https://doi.org/10.1175/2007JCLI1642.1.

Bengtsson, L., K. Hodges, and E. Roeckner, 2006: Storm tracks and climate change. *J. Climate*, **19**, 3518–3543, https://doi.org/10.1175/JCLI3815.1.

Berbery, E. H., 2001: Mesoscale moisture analysis of the North American monsoon. *J. Climate*, **14**, 121–137, https://doi.org/10.1175/1520-0442(2001)013<0121:MMAOTN>2.0.CO;2.

Berrisford, P., P. Kallberg, S. Kobayashi, D. Dee, S. Uppala, A. J. Simmons, P. Poli, and H. Sato, 2011a: Atmospheric conservation properties in ERA-Interim. *Quart. J. Roy. Meteor. Soc.*, **137**, 1381–1399, https://doi.org/10.1002/qj.864.

——, and Coauthors, 2011b: The ERA-Interim archive, version 2.0. ECMWF ERA Tech. Rep. 1, 23 pp., https://www.ecmwf.int/sites/default/files/elibrary/2011/8174-era-interim-archive-version-20.pdf.

Bhattacharya, T., J. E. Tierney, and P. DiNezio, 2017: Glacial reduction of the North American monsoon via surface cooling and atmospheric ventilation. *Geophys. Res. Lett.*, **44**, 5113–5122, https://doi.org/10.1002/2017GL073632.

Bieda, S. W., C. L. Castro, S. L. Mullen, A. C. Comrie, and E. Pytlak, 2009: The relationship of transient upper-level troughs to variability of the North American monsoon system. *J. Climate*, **22**, 4213–4227, https://doi.org/10.1175/2009JCLI2487.1.

Bordoni, S., and B. Stevens, 2006: Principal component analysis of the summertime winds over the Gulf of California: A gulf surge index. *Mon. Wea. Rev.*, **134**, 3395–3414, https://doi.org/10.1175/MWR3253.1.

Brenner, I. S., 1974: A surge of maritime tropical air—Gulf of California to the southwestern United States. *Mon. Wea. Rev.*, **102**, 375–389, https://doi.org/10.1175/1520-0493(1974)102<0375:ASOMTA>2.0.CO;2.

Brewer, M. C., and C. F. Mass, 2016: Projected changes in western U.S. large-scale summer synoptic circulations and variability in CMIP5 models. *J. Climate*, **29**, 5965–5978, https://doi.org/10.1175/JCLI-D-15-0598.1.

Bukovsky, M. S., D. J. Gochis, and L. O. Mearns, 2013: Toward assessing NARCCAP regional climate model credibility for the North American monsoon: Current climate simulations. *J. Climate*, **26**, 8802–8826, https://doi.org/10.1175/JCLI-D-12-00538.1.

Byrne, M. P., and P. A. O'Gorman, 2018: Trends in continental temperature and humidity directly linked to ocean warming. *Proc. Natl. Acad. Sci. USA*, **115**, 4863–4868, https://doi.org/10.1073/pnas.1722312115.

Camargo, S. J., 2013: Global and regional aspects of tropical cyclone activity in the CMIP5 models. *J. Climate*, **26**, 9880–9902, https://doi.org/10.1175/JCLI-D-12-00549.1.

Castro, C. L., R. A. Pielke Sr., and J. O. Adegoke, 2007a: Investigation of the summer climate of the contiguous United States and Mexico using the Regional Atmospheric Modeling System (RAMS). Part I: Model climatology (1950–2002). *J. Climate*, **20**, 3840–3865, https://doi.org/10.1175/JCLI4211.1.

——, S. D. Schubert, and P. J. Pegion, 2007b: Investigation of the summer climate of the contiguous United States and Mexico using the Regional Atmospheric Modeling System (RAMS). Part II: Model climate variability. *J. Climate*, **20**, 3866–3887, https://doi.org/10.1175/JCLI4212.1.

Chang, H.-I., C. L. Castro, C. M. Carrillo, and F. Dominguez, 2015: The more extreme nature of U.S. warm season climate in the recent observational record and two "well-performing" dynamically downscaled CMIP3 models. *J. Geophys. Res. Atmos.*, **120**, 8244–8263, https://doi.org/10.1002/2015JD023333.

Chen, M., W. Shi, P. Xie, V. B. S. Silva, V. E. Kousky, R. W. Higgins, and J. E. Janowiak, 2008a: Assessing objective techniques for gauge-based analyses of global daily precipitation. *J. Geophys. Res.*, **113**, D04110, https://doi.org/10.1029/2007JD009132.

——, and Coauthors, 2008b: CPC unified gauge-based analysis of global daily precipitation. *Western Pacific Geophysics Meeting*, Cairns, Australia, Amer. Geophys. Union, http://ftp.cpc.ncep.noaa.gov/precip/CPC_UNI_PRCP/GAUGE_GLB/DOCU/Chen_et_al_2008_Daily_Gauge_Anal.pdf.

Christidis, N., and P. A. Stott, 2015: Changes in the geopotential height at 500 hPa under the influence of external climatic forcings. *Geophys. Res. Lett.*, **42**, 10 798–10 806, https://doi.org/10.1002/2015GL066669.

Cook, B. I., and R. Seager, 2013: The response of the North American monsoon to increased greenhouse gas forcing. *J. Geophys. Res. Atmos.*, **118**, 1690–1699, https://doi.org/10.1002/jgrd.50111.

Crimmins, M. A., 2006: Arizona and the North American monsoon system. University of Arizona Cooperative Extension, AZ1417, https://extension.arizona.edu/sites/extension.arizona.edu/files/pubs/az1417.pdf.

Dee, D. P., and Coauthors, 2011: The ERA-Interim reanalysis: Configuration and performance of the data assimilation system. *Quart. J. Roy. Meteor. Soc.*, **137**, 553–597, https://doi.org/10.1002/qj.828.

Delworth, T. L., and F. Zeng, 2014: Regional rainfall decline in Australia attributed to anthropogenic greenhouse gases and ozone levels. *Nat. Geosci.*, **7**, 583–587, https://doi.org/10.1038/ngeo2201.

——, and Coauthors, 2012: Simulated climate and climate change in the GFDL CM2.5 high-resolution coupled climate model. *J. Climate*, **25**, 2755–2781, https://doi.org/10.1175/JCLI-D-11-00316.1.

——, F. Zeng, G. A. Vecchi, X. Yang, L. Zhang, and R. Zhang, 2016: The North Atlantic Oscillation as a driver of rapid climate change in the Northern Hemisphere. *Nat. Geosci.*, **9**, 509–512, https://doi.org/10.1038/ngeo2738.

Douglas, M. W., R. A. Maddox, K. Howard, and S. Reyes, 1993: The Mexican monsoon. *J. Climate*, **6**, 1665–1667, https://doi.org/10.1175/1520-0442(1993)006<1665:TMM>2.0.CO;2.

Duchon, C. E., 1979: Lanczos filtering in one and two dimensions. *J. Appl. Meteor.*, **18**, 1016–1122, https://doi.org/10.1175/1520-0450(1979)018<1016:LFIOAT>2.0.CO;2.

Erfani, E., and D. Mitchell, 2014: A partial mechanistic understanding of the North American monsoon. *J. Geophys. Res. Atmos.*, **119**, 13 096–13 115, https://doi.org/10.1002/2014JD022038.

Favors, J. E., and J. T. Abatzoglou, 2013: Regional surges of monsoonal moisture into the southwestern United States. *Mon. Wea. Rev.*, **141**, 182–191, https://doi.org/10.1175/MWR-D-12-00037.1.

Finch, Z. O., and R. H. Johnson, 2010: Observational analysis of an upper-level inverted trough during the 2004 North American Monsoon Experiment. *Mon. Wea. Rev.*, **138**, 3540–3555, https://doi.org/10.1175/2010MWR3369.1.

Fuller, R. D., and D. J. Stensrud, 2000: The relationship between tropical easterly waves and surges over the Gulf of California during the North American monsoon. *Mon. Wea. Rev.*, **128**, 298–306, https://doi.org/10.1175/1520-0493(2000)128<2983:TRBTEW>2.0.CO;2.

Geil, K. L., Y. L. Serra, and X. Zeng, 2013: Assessment of CMIP5 model simulations of the North American monsoon system. *J. Climate*, **26**, 8787–8801, https://doi.org/10.1175/JCLI-D-13-00044.1.

Hales, J. E., Jr., 1972: Surges of maritime tropical air northward over the Gulf of California. *Mon. Wea. Rev.*, **100**, 2983–2989, https://doi.org/10.1175/1520-0493(1972)100<0298:SOMTAN>2.3.CO;2.

Harris, L. M., and S.-J. Lin, 2014: Global-to-regional nested grid climate simulations in the GFDL High Resolution Atmospheric Model. *J. Climate*, **27**, 4890–4910, https://doi.org/10.1175/JCLI-D-13-00596.1.

——, ——, and C. Tu, 2016: High-resolution climate simulations using GFDL HiRAM with a stretched global grid. *J. Climate*, **29**, 4293–4314, https://doi.org/10.1175/JCLI-D-15-0389.1.

Higgins, R. W., Y. Yao, and X. L. Wang, 1997: Influence of the North American monsoon system on the U.S. summer precipitation regime. *J. Climate*, **10**, 298–306, https://doi.org/10.1175/1520-0442(1997)010<2600:IOTNAM>2.0.CO;2.

——, W. Shi, and C. Hain, 2004: Relationships between Gulf of California moisture surges and precipitation in the southwestern United States. *J. Climate*, **17**, 2983–2997, https://doi.org/10.1175/1520-0442(2004)017<2983:RBGOCM>2.0.CO;2.

Huffman, G. J., and Coauthors, 2007: The TRMM Multisatellite Precipitation Analysis (TMPA): Quasi-global, multiyear, combined-sensor precipitation estimates at fine scales. *J. Hydrometeor.*, **8**, 38–55, https://doi.org/10.1175/JHM560.1.

Jiang, X., and N. Lau, 2008: Intraseasonal teleconnection between North American and western North Pacific monsoons with 20-day time scale. *J. Climate*, **21**, 2664–2679, https://doi.org/10.1175/2007JCLI2024.1.

Kapnick, S. B., T. L. Delworth, M. Ashfaq, S. Malyshev, and P. C. D. Milly, 2014: Snowfall less sensitive to warming in Karakoram than in Himalayas due to a unique seasonal cycle. *Nat. Geosci.*, **7**, 834–840, https://doi.org/10.1038/ngeo2269.

Kikuchi, K., and B. Wang, 2009: Global perspective of the quasi-biweekly oscillation. *J. Climate*, **22**, 1340–1359, https://doi.org/10.1175/2008JCLI2368.1.

Kiladis, G. N., and E. A. Hall-McKim, 2004: Intraseasonal modulation of precipitation over the North American monsoon region. *15th Symp. on Global Change and Climate Variations*, Seattle, WA, Amer. Meteor. Soc., 11.4, http://ams.confex.com/ams/pdfpapers/72428.pdf.

King, T. S., and R. C. Balling, 1994: Diurnal variations in Arizona monsoon lightning data. *Mon. Wea. Rev.*, **122**, 1659–1664, https://doi.org/10.1175/1520-0493(1994)122<1659:DVIAML>2.0.CO;2.

Lahmers, T. M., C. L. Castro, D. K. Adams, Y. L. Serra, J. J. Brost, and T. Luong, 2016: Long-term changes in the climatology of transient inverted troughs over the North American monsoon region and their effects on precipitation. *J. Climate*, **29**, 6037–6064, https://doi.org/10.1175/JCLI-D-15-0726.1.

Lee, M.-I., and Coauthors, 2007a: An analysis of the warm-season diurnal cycle over the continental Unites States and northern Mexico in general circulation models. *J. Hydrometeor.*, **8**, 344–366, https://doi.org/10.1175/JHM581.1.

——, and Coauthors, 2007b: Sensitivity to horizontal resolution in the AGCM simulations of warm season diurnal cycle of precipitation over the United States and northern Mexico. *J. Climate*, **20**, 1862–1881, https://doi.org/10.1175/JCLI4090.1.

Liang, X.-Z., J. Zhu, K. E. Kunkel, M. Ting, and J. X. L. Wang, 2008: Do CGCMs simulate the North American monsoon precipitation seasonal–interannual variability? *J. Climate*, **21**, 4424–4448, https://doi.org/10.1175/2008JCLI2174.1.

Lorenz, D. J., and D. L. Hartmann, 2006: The effect of the MJO on the North American monsoon. *J. Climate*, **19**, 333–343, https://doi.org/10.1175/JCLI3684.1.

Luong, T. M., C. L. Castro, H.-I. Chang, T. Lahmers, D. K. Adams, and C. A. Ochoa-Moya, 2017: The more extreme nature of North American monsoon precipitation in the southwestern United States as revealed by a historical climatology of simulated severe weather events. *J. Appl. Meteor. Climatol.*, **56**, 2509–2529, https://doi.org/10.1175/JAMC-D-16-0358.1.

——, ——, T. M. Nguyen, W. W. Cassell, and H.-I. Chang, 2018: Improvement in the modeled representation of North American monsoon precipitation using a modified Kain–Fritsch convective parameterization scheme. *Atmosphere*, **9**, 31, https://doi.org/10.3390/atmos9010031.

Maddox, R. A., D. M. McCollum, and K. W. Howard, 1995: Large-scale patterns associated with severe summertime thunderstorms over central Arizona. *Wea. Forecasting*, **10**, 763–778, https://doi.org/10.1175/1520-0434(1995)010<0763:LSPAWS>2.0.CO;2.

Maloney, E. D., and Coauthors, 2014: North American climate in CMIP5 experiments: Part III: Assessment of twenty-first-century projections. *J. Climate*, **27**, 2230–2270, https://doi.org/10.1175/JCLI-D-13-00273.1.

Mazon, J. J., C. L. Castro, D. K. Adams, H.-I. Chang, C. M. Carrillo, and J. Brost, 2016: Objective climatological analysis of extreme weather events in Arizona during the North American monsoon. *J. Climate Appl. Meteor.*, **55**, 2431–2450, https://doi.org/10.1175/JAMC-D-16-0075.1.

Meehl, G. A., and Coauthors, 2007: Global climate projections. *Climate Change 2007: The Physical Science Basis*, S. Solomon et al., Eds., Cambridge University Press, 747–845.

Mejia, J. F., M. W. Douglas, and P. J. Lamb, 2016: Observational investigation of relationships between moisture surges and mesoscale- to large-scale convection during the North American monsoon. *Int. J. Climatol.*, **36**, 2555–2569, https://doi.org/10.1002/joc.4512.

Meyer, J. D. D., and J. Jin, 2016: Bias correction of the CCSM4 for improved regional climate modeling of the North American monsoon. *Climate Dyn.*, **46**, 2961–2976, https://doi.org/10.1007/s00382-015-2744-5.

Mitchell, D. L., D. Ivanova, R. Rabin, T. J. Brown, and K. Redmond, 2002: Gulf of California sea surface temperatures and the North American monsoon: Mechanistic implications from observations. *J. Climate*, **15**, 2261–2281, https://doi.org/10.1175/1520-0442(2002)015<2261:GOCSST>2.0.CO;2.

Mo, K. C., J.-K. Schemm, H. M. H. Juang, R. W. Higgins, and Y. Song, 2005: Impact of model resolution on the prediction of summer precipitation over the United States and Mexico. *J. Climate*, **18**, 3910–3927, https://doi.org/10.1175/JCLI3513.1.

Moore, A. W., and Coauthors, 2015: National Weather Service forecasters use GPS precipitable water vapor for enhanced situational awareness during the Southern California summer monsoon. *Bull. Amer. Meteor. Soc.*, **96**, 1867–1877, https://doi.org/10.1175/BAMS-D-14-00095.1.

Moorthi, S., and M. J. Suarez, 1992: Relaxed Arakawa–Schubert. A parameterization of moist convection for general circulation models. *Mon. Wea. Rev.*, **120**, 978–1002, https://doi.org/10.1175/1520-0493(1992)120<0978:RASAPO>2.0.CO;2.

Murakami, H., and Coauthors, 2012: Future changes in tropical cyclone activity projected by the new high-resolution

MRI-AGCM. *J. Climate*, **25**, 3237–3260, https://doi.org/10.1175/JCLI-D-11-00415.1.

Newman, A. J., and R. H. Johnson, 2012: Simulation of a North American monsoon gulf surge event and comparison to observations. *Mon. Wea. Rev.*, **140**, 2534–2554, https://doi.org/10.1175/MWR-D-11-00223.1.

——, and ——, 2013: Dynamics of a simulated North American monsoon gulf surge event. *Mon. Wea. Rev.*, **141**, 3238–3253, https://doi.org/10.1175/MWR-D-12-00294.1.

Pascale, S., and S. Bordoni, 2016: Tropical and extratropical controls of Gulf of California surges and summertime precipitation over the southwestern United States. *Mon. Wea. Rev.*, **144**, 2695–2718, https://doi.org/10.1175/MWR-D-15-0429.1.

——, ——, S. B. Kapnick, G. A. Vecchi, L. Jia, T. L. Delworth, S. Underwood, and W. Anderson, 2016: The impact of horizontal resolution on North American monsoon Gulf of California moisture surges in a suite of coupled global climate models. *J. Climate*, **29**, 7911–7936, https://doi.org/10.1175/JCLI-D-16-0199.1.

——, W. R. Boos, S. Bordoni, T. L. Delworth, S. B. Kapnick, H. Murakami, G. A. Vecchi, and W. Zhang, 2017: Weakening of the North American monsoon with global warming. *Nat. Climate Change*, **7**, 806–812, https://doi.org/10.1038/nclimate3412.

Prein, A. F., R. M. Rasmussen, K. Ikeda, C. Liu, M. P. Clark, and G. J. Holland, 2017a: The future intensification of hourly precipitation extremes. *Nat. Climate Change*, **7**, 48–52, https://doi.org/10.1038/nclimate3168.

——, C. Liu, K. Ikeda, S. B. Trier, R. M. Rasmussen, G. J. Holland, and M. P. Clark, 2017b: Increased rainfall volume from future convective storms in the US. *Nat. Climate Change*, **7**, 880–884, https://doi.org/10.1038/s41558-017-0007-7.

Ralph, F. M., and Coauthors, 2014: A vision for future observations for western U.S. extreme precipitation and flooding. *J. Contemp. Water Res. Educ.*, **153**, 16–32, https://doi.org/10.1111/j.1936-704X.2014.03176.x.

Ray, A. J., G. M. Garfin, M. Wilder, M. Vasquez-León, M. Lenart, and A. C. Comrie, 2007: Applications of monsoon research: Opportunities to inform decision making and reduce regional vulnerability. *J. Climate*, **20**, 1608–1627, https://doi.org/10.1175/JCLI4098.1.

Rienecker, M. M., and Coauthors, 2011: MERRA: NASA's Modern-Era Retrospective Analysis for Research and Applications. *J. Climate*, **24**, 3624–3648, https://doi.org/10.1175/JCLI-D-11-00015.1.

Rogers, P. J., and R. H. Johnson, 2007: Analysis of the 13–14 July gulf surge event during the 2004 North American Monsoon Experiment. *Mon. Wea. Rev.*, **135**, 3098–3117, https://doi.org/10.1175/MWR3450.1.

Ryu, J.-H., and K. Hayhoe, 2014: Understanding the sources of Caribbean precipitation biases in CMIP3 and CMIP5 simulations. *Climate Dyn.*, **42**, 3233–3252, https://doi.org/10.1007/s00382-013-1801-1.

Schiffer, N. J., and S. W. Nesbitt, 2012: Flow, moisture, and thermodynamic variability associated with Gulf of California surges within the North American monsoon. *J. Climate*, **25**, 4220–4241, https://doi.org/10.1175/JCLI-D-11-00266.1.

Schmitz, J. T., and S. L. Mullen, 1996: Water vapor transport associated with the summertime North American monsoon as depicted by ECMWF analyses. *J. Climate*, **9**, 1621–1634, https://doi.org/10.1175/1520-0442(1996)009<1621:WVTAWT>2.0.CO;2.

Schneider, U., A. Becker, P. Finger, A. Meyer-Christoffer, M. Ziese, and B. Rudolf, 2014: GPCC's new land surface precipitation climatology based on quality-controlled in situ data and its role in quantifying the global water cycle. *Theor. Appl. Climatol.*, **115**, 15–40, https://doi.org/10.1007/s00704-013-0860-x.

Seastrand, S., Y. Serra, C. Castro, and E. Ritchie, 2015: The dominant synoptic-scale modes of North American monsoon precipitation. *Int. J. Climatol.*, **35**, 2019–2032, https://doi.org/10.1002/joc.4104.

Serra, Y. L., and K. Geil, 2017: Historical and projected eastern Pacific and intra-Americas sea TD-wave activity in a selection of IPCC AR5 models. *J. Climate*, **30**, 2269–2294, https://doi.org/10.1175/JCLI-D-16-0453.1.

Seth, A., S. A. Rauscher, M. Rojas, A. Giannini, and S. J. Camargo, 2011: Enhanced spring convective barrier for monsoons in a warmer world? *Climatic Change*, **104**, 403–414, https://doi.org/10.1007/s10584-010-9973-8.

Stensrud, D. J., R. L. Gall, and M. K. Nordquist, 1997: Surges over the Gulf of California during the Mexican monsoon. *Mon. Wea. Rev.*, **125**, 417–437, https://doi.org/10.1175/1520-0493(1997)125<0417:SOTGOC>2.0.CO;2.

Svoma, B. M., 2010: The influence of monsoonal gulf surges on precipitation and diurnal precipitation patterns in central Arizona. *Wea. Forecasting*, **25**, 281–289, https://doi.org/10.1175/2009WAF2222299.1.

Taylor, K. E., R. J. Stouffer, and G. A. Meehl, 2012: An overview of CMIP5 and the experiment design. *Bull. Amer. Meteor. Soc.*, **95**, 485–498, https://doi.org/10.1175/BAMS-D-11-00094.1.

Torres-Alavez, A., T. Cavazos, and C. Turrent, 2014: Land–sea thermal contrast and intensity of the North American monsoon under climate change conditions. *J. Climate*, **27**, 4566–4580, https://doi.org/10.1175/JCLI-D-13-00557.1.

Tripathi, O. P., and F. Dominguez, 2013: Effects of spatial resolution in the simulation of daily and subdaily precipitation in the southwestern US. *J. Geophys. Res. Atmos.*, **118**, 7591–7605, https://doi.org/10.1002/jgrd.50590.

van der Wiel, K., and Coauthors, 2016: The resolution dependence of contiguous U.S. precipitation extremes in response to CO_2 forcing. *J. Climate*, **29**, 7991–8012, https://doi.org/10.1175/JCLI-D-16-0307.1.

Vecchi, G. A., and Coauthors, 2014: On the seasonal forecasting of regional tropical cyclone activity. *J. Climate*, **27**, 7994–8016, https://doi.org/10.1175/JCLI-D-14-00158.1.

Wang, C., S. Lee, and D. Enfield, 2007: Impact of the Atlantic warm pool on the summer climate of the Western Hemisphere. *J. Climate*, **20**, 5021–5040, https://doi.org/10.1175/JCLI4304.1.

WMO, 2008: Guide to meteorological instruments and methods of observation. 7th ed., WMO 8, 716 pp., http://library.wmo.int/pmb_ged/wmo_8_en-2012.pdf.

Yang, L., J. Smith, M. L. Baeck, E. Morin, and D. C. Goodrich, 2017: Flash flooding in arid/semiarid regions: Dissecting the hydrometeorology and hydrology of the 19 August 2014 storm and flood hydroclimatology in Arizona. *J. Hydrometeor.*, **18**, 3103–3123, https://doi.org/10.1175/JHM-D-17-0089.1.

Zehnder, J. A., 2004: Dynamic mechanisms of the gulf surge. *J. Geophys. Res.*, **109**, D10107, https://doi.org/10.1029/2004JD004616.

Zhang, H., T. Delworth, F. Zeng, G. Vecchi, K. Paffendorf, and L. Jia, 2016: Detection, attribution, and projection of regional rainfall changes on (multi-) decadal time scales: A focus on southeastern South America. *J. Climate*, **29**, 8515–8534, https://doi.org/10.1175/JCLI-D-16-0287.1.